Networks and Heterogeneous Media

https://www.aimspress.com/journal/nhm

NHM, 21(3): 865–893.
DOI: 10.3934/nhm.2026036
Received: 24 November 2025
Revised: 24 April 2026
Accepted: 28 April 2026
Published: 07 May 2026

Research article

Abundant new lump type interaction wave solutions and nonlinear dynamics for the (4+1)-dimensional Fokas equation

Junjie Li[1], **Pei Lin**[2], **Xin Zhen**[1] **and Junjiang Zhong**[1,*]

[1] School of Mathematics and Statistics, Xiamen University of Technology, Xiamen 361024, China

[2] College of Computer and Information Engineering, Xiamen University of Technology, Xiamen 361024, China

* **Correspondence:** Email: jjzhong@xmut.edu.cn.

Abstract: In this paper, the (4+1)-dimensional Fokas equation is first reduced to a (2+1)-dimensional bilinear form, and then analyzed by an architecture-guided bilinear neural network method (BNNM) within the Hirota framework. Three representative network topologies, namely the "3-2-1", "3-3-1", and "3-2-3-1" configurations, are used to organize trial functions and derive exact solutions through symbolic coefficient matching. As a result, several families of exact wave patterns are obtained, including lump solutions, lump–stripe-type solutions, lump–soliton-type solutions, and selected degenerate/high-amplitude structures. The comparison among different architectures shows that the hidden-layer depth and the activation composition affect the admissible ansatz forms and the morphology of the resulting interaction profiles for the reduced Fokas equation. The derived solutions are interpreted as prototype wave patterns and analytical benchmarks for localization, interaction, and modulation in multidimensional dispersive media, rather than as experimentally calibrated predictions. In addition, an auxiliary Duffing-based modulation diagnostic is used to visualize the irregular modulation of one selected high-amplitude profile; this comparison is qualitative and does not constitute a rigorous proof that the reduced Fokas equation itself is chaotic. These results show that the BNNM framework provides a structured symbolic route to construct and compare the exact interaction solutions of the reduced Fokas equation.

Keywords: Fokas equation; neural network; analytical solutions; Hirota bilinear method

1. Introduction

Nonlinear Evolution Equations (NLEEs) serve as fundamental mathematical tools to describe complex nonlinear phenomena in nature. They exert a crucial influence in many fields, including fluid dynamics, plasma physics, nonlinear optics, and geophysics [1–3]. These equations can accurately

characterize dynamic processes such as wave propagation, energy transfer, and interfacial interactions. Their exact solutions are essential to reveal the intrinsic mechanisms of nonlinear systems. Additionally, they provide important theoretical support to predict practical physical phenomena, such as oceanic rogue waves, optical pulse transmission, and shallow-water wave dynamics [4–6]. Owing to their ability to reflect the multidimensional features of realistic physical scenarios, high-dimensional NLEEs, in particular, have attracted increasing attention in nonlinear science [7, 8].

Since the 20th century, researchers have developed a variety of effective analytical methods to construct exact solutions, including the Darboux transformation [9, 10], a Lie symmetry analysis [11, 12], the Hirota bilinear method [13, 14], the Bell polynomial approach [15, 16], and the extended direct algebraic method [17, 18]. Among these approaches, the Hirota bilinear method is adopted in the present study because of its inherent simplicity, strong applicability, and efficiency in transforming nonlinear evolution equations into bilinear forms. Wang et al. employ the Hirota bilinear method to uncover new multi-rogue waves, breathers, bell-shaped, and singular waveforms for the (3+1)-dimensional Yu–Toda–Sasa–Fukuyama equation [19]. Moreover, Wang and collaborators investigated diverse exact wave structures—including N-solitons, lumps, and soliton molecules—for the Kairat-II-X equation in plasma physics, while Wang separately formulated a fractal physics-informed neural network scheme to accurately model exothermic reactions in porous media [20, 21]. The integration of deep learning and traditional analytical methods has opened up new research directions [22, 23], which can be attributed to the rapid progress of artificial intelligence. Physics-Informed Neural Networks (PINNs) were among the earliest frameworks to embed physical laws into neural network training. However, they often face difficulties in achieving high-precision exact solutions and typically incur high computational costs [24]. In contrast, the bilinear neural network method (BNNM), proposed by combining the Hirota bilinear method with neural network architectures, has emerged as a powerful technique to obtain exact analytical solutions [25–27]. Recent investigations presented a novel Bernoulli sub-equation neural network scheme, wherein the solutions derived from the Bernoulli sub-equation were utilized as the activation mechanism within the first hidden layer to formulate trial functions, thereby enabling the extraction of previously unidentified exact traveling wave patterns for the Cahn–Allen equation [28]. This method encompasses the most traditional bilinear-based construction strategies. By optimizing the activation functions and network topologies, it can effectively reduce the high computational cost of symbolic methods when treating complex interaction solutions [29]. Unlike traditional methods, BNNM not only generates exact expressions but also reveals the coupling mechanisms between different wave patterns, such as lumps, stripes, and solitons. By analyzing these interaction solutions, we gain more insights into how energy localization and dispersion processes co-evolve in the Fokas system. Moreover, as the number of variables continues to grow, dimensionality reduction for high-dimensional nonlinear partial differential equations (NPDEs) becomes increasingly crucial. Its core lies in leveraging structural properties of the problem and eliminating redundant dimensions through approaches such as variable separation and symmetry reduction to achieve dimensionality reduction.

It is important to distinguish the present BNNM from physics-informed neural networks (PINNs). PINNs are training-based frameworks to obtain numerical approximate solutions or inverse reconstructions of differential equations through physics-based residual minimization. By contrast,

the present BNNM is a neuro-symbolic exact-solution construction framework: the network topology is only used to organize trial functions and activation compositions within the Hirota bilinear setting, while the coefficients are determined by symbolic matching rather than training. From this viewpoint, the present work is complementary to PINN-type studies rather than a competing numerical solver. Therefore, we cited both standard PINN references and the recent PINN study [21] to make this distinction explicit.

The (4+1)-dimensional Fokas equation is a representative fully integrable high-dimensional model. It can capture complex wave dynamics in multiple spatial–temporal dimensions. Its solution space is of great significance in several areas, including quantum mechanics and marine engineering [30]. Recent works have investigated its solutions using various analytical techniques. Examples include the construction of vectorial Darboux transformation solutions for coupled Fokas–Lenells equations [31, 32], and the derivation of perturbed quiescent optical solitons for Fokas–Lenells equations with generalized nonlinearities [11]. These studies underscore the lasting research value of this equation [30]. For the (4+1)-dimensional Fokas equation and its variants, existing research has yielded a wide range of solutions: Cao et al. [33] obtained localized solitary waves, breather waves, and multisoliton solutions; Zhang et al. [30] discovered novel hybrid solitary waves and shrunken-periodic solutions; and Yildirim et al. [11] retrieved perturbed quiescent optical solitons for Fokas-Lenells equations.

In recent years, research on the exact wave solutions of high-dimensional integrable systems and their derived models has continued to deepen, with remarkable achievements, particularly in seeking complex solutions with localized properties or inelastic collision behavior. For example, Cao et al. [34] studied the Airy function ripple solutions of the generalized (3+1)-dimensional KP equation, thus revealing the dissipative evolution characteristics of solitons over time. For the Maccari system, which is regarded as a two-dimensional generalization of the nonlinear Schrödinger equation, researchers have obtained mixed collision solutions of elastic and inelastic interactions between lump waves and dark solitons [35]. Furthermore, by using the KP reduction method, two-dimensional fully localized rogue waves on a dark soliton background were derived, and the generation conditions for their resonant collisions were clarified [36]. In addition, research on the nonlocal KP equation has proposed partially rogue wave–ripple solutions with semi-local temporal characteristics. These solutions tend to a constant background as the time approaches infinity, which more closely resembles the decay process of actual water waves [37]. In the direct construction of higher-order rogue waves, the literature demonstrates, using the Hirota method for the generalized (3+1)-dimensional model, the regulatory effect of central control parameters on the amplitude and shape of rogue waves [38].

Nevertheless, there is a scarcity of interaction solutions [39], for which BNNM possesses clear advantages in its construction. The contribution of the BNNM construction lies not merely in generating exact expressions, but in providing a structured framework to organize hybrid wave ansatze and to analyze how the activation composition and network depth shape the localization, stripe coupling, and soliton-interaction morphology in the Fokas system. The core value of such studies lies in clarifying the coupling mechanisms between different solitons, waves, or physical modes. This understanding supports the analysis of complex dynamics and practical applications of nonlinear systems (e.g., NPDEs). Therefore, it is necessary to address these gaps. In the present study, attention was focused on a (4+1)-dimensional nonlinear Fokas equation [40], which is

expressed as follows:

$$4u_{x_1t} - u_{x_1x_1x_1x_2} + u_{x_1x_2x_2x_2} + 6(u^2)_{x_1x_2} - 6u_{y_1y_2} = 0, \tag{1.1}$$

where $u = u(x_1, x_2, y_1, y_2, t)$.

Although the parameter sets used in this paper are illustrative rather than experimentally fitted, the obtained exact solutions can still be interpreted as canonical wave patterns for multidimensional dispersive media. In this sense, lump-like profiles represent the localized energy concentration, while stripe-type and soliton-type components describe quasi-one-dimensional carrier structures and interaction channels. Therefore, the present results are better understood as prototype mechanisms and analytical benchmarks for wave localization, interaction, and modulation, rather than as directly calibrated predictions for a specific experiment.

The novelty of the present study does not lie in replacing the Hirota bilinear method itself, which remains a powerful and well-established exact-solution technique. Rather, the contribution lies in employing an architecture-guided BNNM viewpoint to organize richer trial functions within the bilinear framework for the reduced (4+1)-dimensional Fokas equation, and in comparing how single-hidden-layer and double-hidden-layer constructions influence the resulting exact lump-type interaction families in this specific equation setting.

The structure of the paper is organized as follows: in Section 2, the BNNM adopted in the experiments is described in detail, including the network architecture design, the bilinear transformation, and the overall solution procedure; in Section 3, three types of exact solutions obtained from the single hidden layer neural network model are presented, and their dynamic characteristics are analyzed; in Section 4, two types of composite solutions constructed by the double hidden layer neural network model are discussed; in Section 5, the neural network framework is combined with a chaotic system to more effectively detect irregular nonlinear phenomena, and the chaotic behaviors exhibited by the exact solutions are investigated via the Duffing chaotic system; and finally, the study is summarized and potential directions for future work are outlined.

2. Method

Equation (1.1) was solved using the Hirota bilinear method. The introduction of the d-operator can be expressed as follows:

$$D_{p,x_1}^{n_1} \cdots D_{p,x_M}^{n_M} a \cdot b(x_1, \cdots, x_M) = \prod_{i=1}^{M} \left(\frac{\partial}{\partial x_i} + \alpha \frac{\partial}{\partial x_i'} \right)^{n_i} a(x_1, \cdots, x_M) b(x_1', \cdots, x_M') \Big|_{x_1'=x_1,\ldots,x'=x_M}, \tag{2.1}$$

where $n_1, \cdots, n_M$ represents any non-negative integer. For a given integer M, the m-th exponent of α is determined as follows:

$$(\alpha_p)^m = (-1)^{r(m)}, m \equiv r(m) \bmod p, \quad 0 \le r(m) < p. \tag{2.2}$$

Through a dependent variable transformation [39],

$$x = k_1x_1 + k_2x_2, \tag{2.3}$$

$$y = k_3y_1 + k_4y_2, \tag{2.4}$$

the original four spatial coordinates are reduced to two combined coordinates, while the derivative structure required for the subsequent bilinearization is preserved. The dependent-variable transformation is taken as follows:

$$u(x, y, t) = (k_2^2 - k_1^2)\frac{\partial}{\partial x \partial x} \ln f(x, y, t). \tag{2.5}$$

Equation (1.1) can be converted into the following bilinear form:

$$(4D_xD_t + k_2(k_2^2 - k_1^2)D_x^4 - \frac{6k_3k_4}{k_1}D_y^2)f \cdot f = 0. \tag{2.6}$$

This choice of reduction is consistent with the standard treatment of the (4+1)-dimensional Fokas equation in the literature [39], and the Eq (2.6) is equivalent to the following:

$$8ff_{xt} - 8f_xf_t + 2k_2(k_2^2 - k_1^2)(ff_{xxxx} - 4f_xf_{xxx} + 3f_{xx}^2) - \frac{12k_3k_4}{k_1}ff_{yy} + \frac{12k_3k_4}{k_1}f_y^2 = 0. \tag{2.7}$$

The Hirota bilinear transformation was employed in the aforementioned equations to effectively strengthen the nonlinear terms of the system. A higher-order rational function relating f and its derivatives was introduced to enhance the nonlinear features of the equation, thereby enabling a more accurate description of complex dynamical phenomena. Owing to its intrinsic binary structure, the transformed equation is particularly well suited to the BNNM framework adopted in the present study. In order to obtain the exact analytical solutions of Eq (2.6), the tensor formula employed in the neural network of the present study is expressed as follows:

$$f = \omega_{l_n,f}F_{l_n}(\xi_{l_n}), \tag{2.8}$$

where $\omega_{l_n,f}$ signifies the weight coefficient linking neuron l_n to f. The function F signifies a generalized activation function utilized to modulate the network's nonlinear characteristics, which can be defined in multiple ways. The set $l_n = \{m_{n-1} + 1, m_{n-1} + 2, \ldots, n\}$ denotes the neuron space that corresponds to the n-th layer of the neural network, which guarantees a unambiguous hierarchical structure and well-specified recursive computations. The parameter ξ_l is formulated as follows:

$$\xi_{l_i} = \omega_{l_{i-1},l_i}F_{l_{i-1}}(\xi_{l_{n-1}}) + b_{l_i}, i = 1, 2, \ldots, n, \tag{2.9}$$

where $l_0 = \{x, y, t\}, l_1 = \{1, 2, \ldots, m_1\}$, and $l_i = \{m_{i-1} + 1, m_{i-1} + 2, \ldots, m_i\}$. l_0 represents the input layer, l_1 defines the neurons of the first layer, l_i specifies the neurons in the i-th layer, and b_{l_i} represents a bias term that is treated as a constant in the computation process. The neural network architecture employed in the present study is shown in Figure 1.

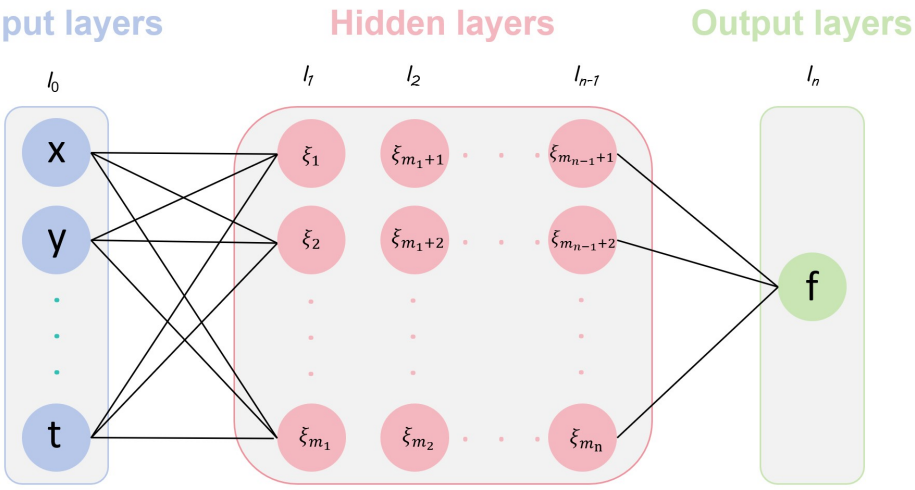

Figure 1. Neural network model of Eq (2.8).

Through the BNNM, several hidden layers can be incorporated, which aids in strengthening their expressive ability and improving the expressive capacity. In the present research, three distinct architectures of neural networks are investigated. By means of this systematic approach, the aim is to obtain precise analytical solutions for the generalized (4+1)-dimensional Fokas equation.

It is worth emphasizing that the bilinear neural network approach described here is not intended as a substitute for the Hirota bilinear method itself. The Hirota framework remains the essential analytical foundation to generate exact solutions. Rather, the difficulty, is that when the interaction patterns become more complicated, constructing effective trial functions by hand becomes increasingly impractical. Therefore, our use of the term "neural network" is structural rather than algorithmic: we only borrow the organizing logic of network topology and activation composition to build richer ansätze, while all coefficients are determined by symbolic consistency conditions rather than by training. In this sense, the present BNNM should be regarded as a neuro-symbolic extension of ansatz construction within the Hirota bilinear setting.

3. Solutions under the architecture of a single hidden layer neural network

As discussed in this section, a neural network structure with a single hidden layer was employed. Unless otherwise stated, the parameter sets used in the figures are illustrative values selected to satisfy the algebraic constraints and to display representative solution morphologies; they are not fitted to a specific experiment. Through comprehensive computations, the exact analytical solutions of Eq (2.6) were generated as follows.

3.1. Lump solutions

The neural network structure was employed as follows:

$$\begin{aligned} f &= \omega_{1,f}\xi_1^2 + \omega_{2,f}\xi_2^2 + b_3, \\ \xi_1 &= \omega_{x,1}x + \omega_{y,1}y + \omega_{t,1}t + b_1, \\ \xi_2 &= \omega_{x,2}x + \omega_{y,2}y + \omega_{t,2}t + b_2, \end{aligned} \tag{3.1}$$

where b_k $(k = 1, 2, 3)$ and $\omega_{i,j}$ ($i = x, y, t, 1, 2$ and $j = 1, 2, f$) are real constants. The "3-2-1" neural network architecture is depicted in Figure 2.

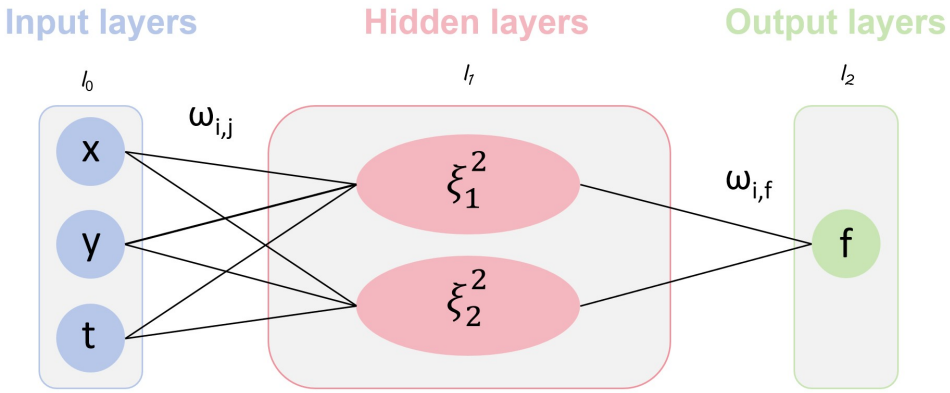

Figure 2. "3-2-1" neural network model.

By substituting Eq (3.1) into Eq (2.6), a complex equation could be obtained. By equating the coefficients to zero and ensuring $\omega_{1,f}, \omega_{2,f} \neq 0$, a system that consists of 10 coefficient equations was derived. With the use of Maple, which is a classic computational tool, two sets of solutions were obtained.
Case 1:

$$\begin{aligned} &\omega_{1,f} = -\frac{\omega_{2,f}\omega_{x,2}^2}{\omega_{x,1}^2}, \omega_{2,f} = \omega_{2,f}, \omega_{t,1} = \frac{3k_3k_4\omega_{y,2}^2\omega_{x,1}}{2k_1\omega_{x,2}^2}, \omega_{t,2} = \frac{3k_3k_4\omega_{y,2}^2}{2k_1\omega_{x,2}}, \\ &\omega_{y,1} = \frac{\omega_{x,1}\omega_{y,2}}{\omega_{x,2}}, \omega_{y,2} = \omega_{y,2}. \end{aligned} \tag{3.2}$$

Case 2:

$$k_4 = 0, b_3 = 0, \omega_{1,f} = -\frac{\omega_{2,f}\omega_{x,2}^2}{\omega_{x,1}^2}, \omega_{t,1} = -\frac{\omega_{t,2}\omega_{x,1}}{\omega_{x,2}}. \tag{3.3}$$

By substituting $Case1$ into Eq (3.1) and applying the bilinear transformation of Eq (2.5), the lump solution of Eq (2.6) could be obtained as follows:

$$\begin{aligned} f &= -\frac{\omega_{2,f}\omega_{x,2}^2}{\omega_{x,1}^2}\phi_1 + \omega_{2,f}\phi_2 + b3, \\ u &= -\frac{(k_2^2 - k_1^2)(\phi_3 + \phi_4)^2}{f^2}, \end{aligned} \tag{3.4}$$

where

$$\phi_1 = (\frac{3tk_3k_4\omega_{y,2}^2\omega_{x,1}}{2k_1\omega_{x,2}^2} + \omega_{x,1}x + \frac{\omega_{x,1}\omega_{y,2}y}{\omega_{x,2}} + b_1)^2,$$
$$\phi_2 = (\frac{3k_3k_4\omega_{y,2}^2t}{2k_1\omega_{x,2}} + \omega_{x,2}x + \omega_{y,2}y + b_2)^2,$$
$$\phi_3 = -\frac{2(\frac{3tk_3k_4\omega_{y,2}^2\omega_{x,1}}{2k_1\omega_{x,2}^2} + \omega_{x,1}x + \frac{\omega_{x,1}\omega_{y,2}y}{\omega_{x,2}} + b_1)\omega_{2,f}\omega_{x,2}^2}{\omega_{x,1}},$$
$$\phi_4 = 2(\frac{3k_3k_4\omega_{y,2}^2t}{2k_1\omega_{x,2}} + \omega_{x,2}x + \omega_{y,2}y + b_2)\omega_{2,f}\omega_{x,2}.$$

For the purpose of comprehensively analyzing the lump solution, systematic numerical studies were performed to explore both its dynamic properties and its evolutionary characteristics. Subsequently, the following parameter was selected and substituted into Eq (3.4):

$$\begin{aligned} &b_1 = 2, b_2 = 2, b_3 = 3, k_1 = 1, k_2 = 2, k_3 = 1, \\ &k_4 = 1, \omega_{2,f} = 1, \omega_{x,1} = 2, \omega_{x,2} = 1, \omega_{y,2} = 3. \end{aligned} \tag{3.5}$$

Figure 3 demonstrates the 3D plot with $t = 0$, the density plot with $t = 0$, and the line plot with $y = 0$, $t = -1$ (red), $t = 0$ (blue), and $t = 1$ (green). The substituted parameter is Eq (3.5). The 3D plot clearly illustrates the localized spatial distribution of the solutions. The density plot intuitively reveals concentrated energy regions with pronounced gradient variations. The line plot provides detailed information on waveform oscillations along different cross-sections. These plots show a localized wave packet with a concentrated amplitude near the interaction center. This morphology may be viewed as a prototype of localized energy concentration in multidimensional dispersive-wave media.

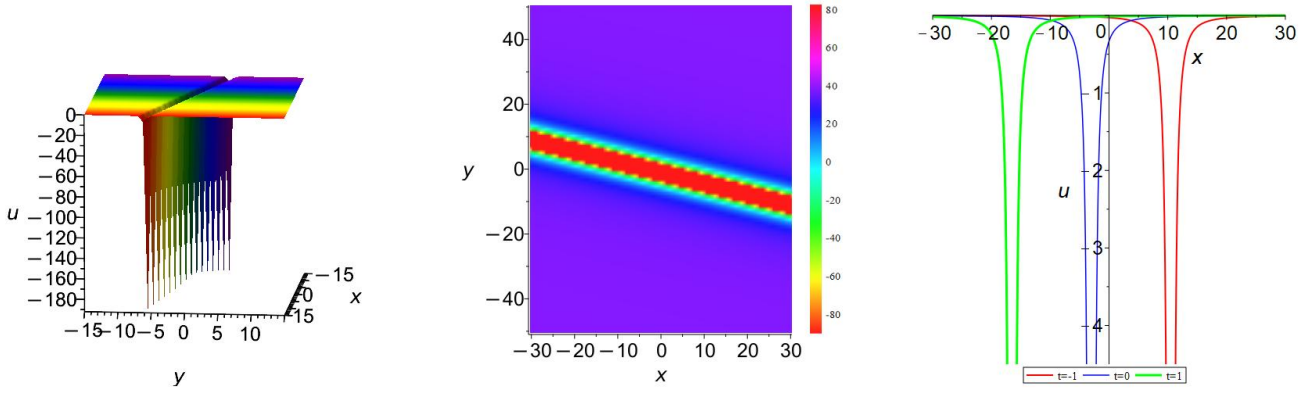

(a) 3D plot **(b)** density plot **(c)** line plot

Figure 3. The 3D plot, density plot, and line plot of lump-type solution.

By substituting *Case*2 into Eq (3.1) and applying the bilinear transformation of Eq (2.5), the lump

solution of Eq (2.6) could be obtained as follows:

$$\begin{aligned} f &= -\frac{\omega_{2,f}\omega_{x,2}^2}{\omega_{x,1}^2}\phi_1 + \omega_{2,f}\phi_2, \\ u &= -\frac{(k_2^2 - k_1^2)(\phi_3 + \phi_4)^2}{f^2}, \end{aligned} \tag{3.6}$$

where

$$\begin{aligned} \phi_1 &= (-\frac{t\omega_{t,2}\omega_{x,1}}{\omega_{x,2}} + \omega_{x,1}x + \omega_{y,1}y + b_1)^2, \\ \phi_2 &= (\omega_{t,2}t + \omega_{x,2}x + \omega_{y,2}y + b_2)^2, \\ \phi_3 &= -\frac{2(-\frac{t\omega_{t,2}\omega_{x,1}}{\omega_{x,2}} + \omega_{x,1}x + \omega_{y,1}y + b_1)\omega_{2,f}\omega_{x,2}^2}{\omega_{x,1}}, \\ \phi_4 &= 2(\omega_{t,2}t + \omega_{x,2}x + \omega_{y,2}y + b_2)\omega_{2,f}\omega_{x,2}. \end{aligned}$$

For the purpose of comprehensively analyzing the lump solution, systematic numerical studies were performed to explore both its dynamic properties and its evolutionary characteristics. Subsequently, the following parameter was selected and substituted into Eq (3.6):

$$\begin{aligned} &b_1 = 3, b_2 = 2, k_1 = 2, k_2 = 1, k_3 = 3, \omega_{2,f} = 1, \\ &\omega_{t,2} = 1, \omega_{x,1} = 3, \omega_{x,2} = 2, \omega_{y,1} = 1, \omega_{y,2} = 3. \end{aligned} \tag{3.7}$$

Figure 4 illustrates the 3D plot with $t = 0$, the density plot with $t = 0$, and the line plot with $y = 0$ and $t = 1$. By substituting Eq (3.7), a 3D plot with a distinctive multi-peak clustered morphology was generated, along with a density plot that displays discrete high-energy patches and line graphs that reveal alternating peak-valley structures. The clustered multi-peak pattern may be interpreted as a representative interaction of several localized components on a structured background, rather than as a directly calibrated model of a specific experiment.

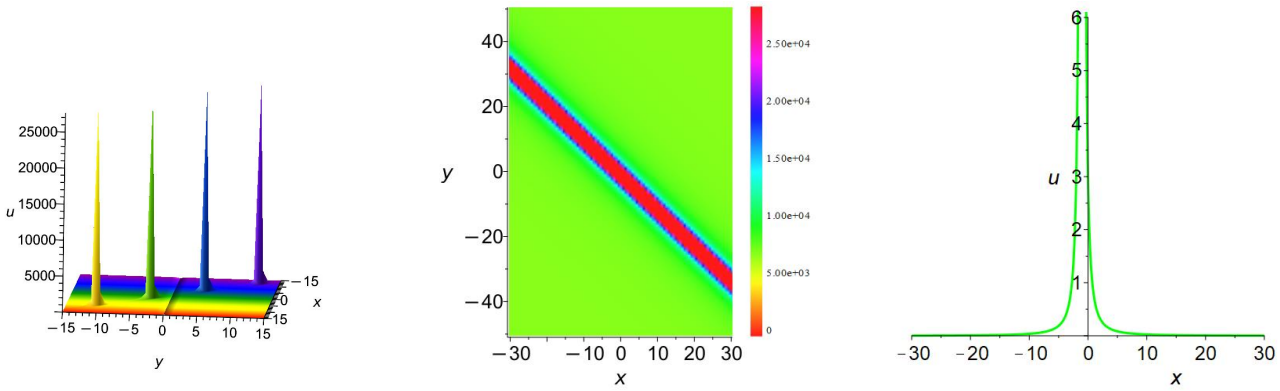

(a) 3D plot **(b)** density plot **(c)** line plot

Figure 4. The 3D plot, density plot, and line plot of lump-type solution.

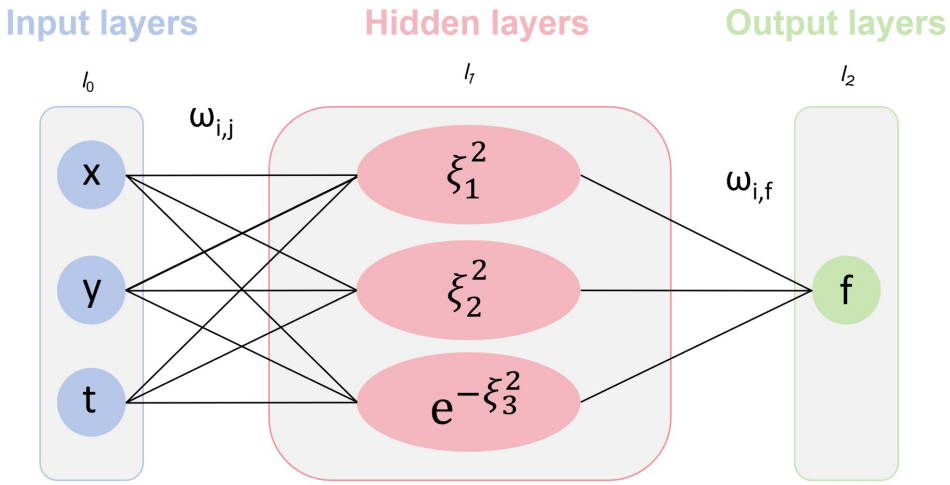

Figure 5. "3-3-1" Neural network model.

3.2. Lump-stripe solutions

To generate the lump–stripe solution, a single hidden layer neural network with a "3-3-1" architecture was employed. This structure consisted of an input layer with three neurons, one hidden layer with three neurons, and one output layer. An additional Gaussian function node is incorporated to enhance the neural network in three main aspects: First, a more diversified activation function set was introduced, thus enabling the network to capture features across different scales and distributions; second, the increase in hidden nodes from two to three enhanced the model complexity and ansatz flexibility, thus improving its solution-construction range; and third, the expansion of the hidden layer effectively enlarged the solution-construction range, thus allowing the network to achieve a structural richness of the trial functions. As a result, the model became more adaptable to complex tasks and more capable of identifying fine-grained patterns in the data. The "3-3-1" neural network structure was employed as follows:

$$\begin{aligned} f &= \omega_{1,f}F_1(\xi_1,\xi_2,\xi_3) + \omega_{2,f}F_2(\xi_1,\xi_2,\xi_3) + \omega_{3,f}F_3(\xi_1,\xi_2,\xi_3) + b_4,\\ \xi_1 &= \omega_{x,1}x + \omega_{y,1}y + \omega_{t,1}t + b_1,\\ \xi_2 &= \omega_{x,2}x + \omega_{y,2}y + \omega_{t,2}t + b_2,\\ \xi_3 &= \omega_{x,3}x + \omega_{y,3}y + \omega_{t,3}t + b_3, \end{aligned} \tag{3.8}$$

where b_k $(k = 1, 2, 3, 4)$ and $\omega_{i,j}$ $(i = x, y, t, 1, 2, 3$ and $j = 1, 2, 3, f)$ are real constants. The activation functions that remain to be identified are the functions $F_i(\xi_1, \xi_2, \xi_3)$ $(i = 1, 2, 3)$. The "3-3-1" neural network architecture is depicted in Figure 5.

$F_1(\xi_1, \xi_2, \xi_3) = \xi_1^2$, $F_2(\xi_1, \xi_2, \xi_3) = \xi_2^2$, and $F_3(\xi_1, \xi_2, \xi_3) = e^{-\xi_3^2}$ are chosen to act as activation functions. By substituting Eq (3.8) to Eq (2.6), a complex equation was obtained. By equating the coefficients to zero and ensuring $\omega_{1,f}, \omega_{2,f}, \omega_{3,f} \neq 0$, a system that consists of 20 coefficient equations was derived. With the use of Maple, which is a classic computational tool, three sets of solutions were obtained.

Case 1:

$$k_2 = 0, k_3 = 0, \omega_{t,1} = 0, \omega_{t,2} = 0, \omega_{t,3} = 0, \omega_{x,1} = 0. \tag{3.9}$$

Case 2:

$$k_2 = 0, k_4 = 0, \omega_{t,1} = 0, \omega_{t,2} = 0, \omega_{t,3} = 0, \omega_{x,1} = 0. \tag{3.10}$$

Case 3:

$$k_2 = 0, \omega_{t,1} = \frac{3k_3k_4\omega_{y,1}^2}{2k_1\omega_{x,1}}, \omega_{t,2} = \frac{3k_3k_4\omega_{y,1}^2\omega_{x,2}}{2\omega_{x,1}^2k_1}, \omega_{t,3} = 0, \omega_{x,3} = 0, \omega_{y,2} = \frac{\omega_{x,2}\omega_{y,1}}{\omega_{x,1}}, \omega_{y,3} = 0. \tag{3.11}$$

By substituting *Case* 1 into Eq (3.8) and applying the bilinear transformation of Eq (2.5), the lump-stripe solution of Eq (2.6) could be obtained as follows:

$$\begin{aligned} f &= \omega_{1,f}\phi_1 + \omega_{2,f}\phi_2 + \omega_{3,f}\phi_3 + b_4, \\ u &= (k_2^2 - k_1^2)(\frac{\phi_4}{f} - \frac{\phi_5}{f^2}), \end{aligned} \tag{3.12}$$

where

$$\begin{aligned} \phi_1 &= (\omega_{y,1}y + b1)^2, \\ \phi_2 &= (\omega_{x,2}x + \omega_{y,2}y + b_2)^2, \\ \phi_3 &= e^{-\omega_{x,3}x - \omega_{y,3}y - b_3}, \\ \phi_4 &= 2\omega_{2,f}\omega_{x,2}^2 + \omega_{3,f}\omega_{x,3}^2\phi_3, \\ \phi_5 &= (2\omega_{2,f}(\omega_{x,2}x + \omega_{y,2}y + b_2)\omega_{x,2} - \omega_{3,f}\omega_{x,3}\phi_3)^2. \end{aligned}$$

For the purpose of comprehensively analyzing the lump-stripe solution, systematic numerical studies were performed to explore both its dynamic properties and its evolutionary characteristics. Subsequently, the following parameter was selected and substituted into Eq (3.12):

$$\begin{aligned} &b_1 = 1, b_2 = 2, b_3 = 3, b_4 = 2, k_1 = 1, k_4 = 3, \\ &\omega_{1,f} = 1, \omega_{2,f} = 2, \omega_{3,f} = 2, \omega_{x,2} = 1, \omega_{x,3} = 1, \omega_{y,1} = 3, \\ &\omega_{y,2} = 3, \omega_{y,3} = 1. \end{aligned} \tag{3.13}$$

Figure 6 demonstrates the 3D plot with $t = 0$, the density plot with $t = 0$, and the line plot with $y = 0$ and $t = 0$. The substituted parameter is shown in Eq (3.13). The coexistence of a localized core and an elongated stripe component provides a qualitative prototype for interactions between localized disturbances and quasi-one-dimensional carrier waves.

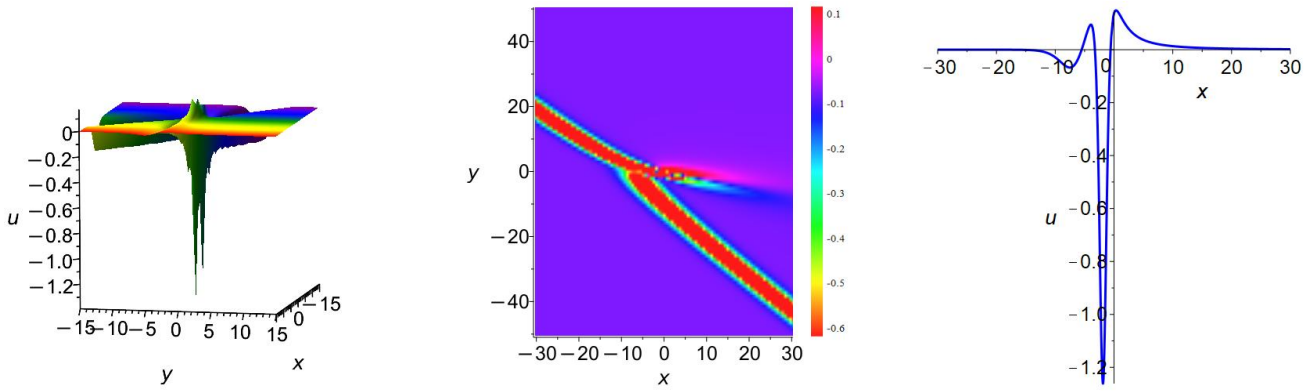

(a) 3D plot **(b)** density plot **(c)** line plot

Figure 6. The 3D plot, density plot, and line plot of lump-stripe solution.

By substituting *Case* 2 into Eq (3.8) and applying the bilinear transformation of Eq (2.5), the lump-stripe solution of Eq (2.6) could be obtained as follows:

$$\begin{aligned} f &= \omega_{1,f}\phi_1 + \omega_{2,f}\phi_2 + \omega_{3,f}\phi_3 + b_4, \\ u &= (k_2^2 - k_1^2)(\frac{\phi_4}{f} - \frac{\phi_5}{f^2}), \end{aligned} \tag{3.14}$$

where

$$\begin{aligned} \phi_1 &= (\omega_{y,1} + b_1)^2, \\ \phi_2 &= (\omega_{x,2}x + \omega_{y,2}y + b_2)^2, \\ \phi_3 &= e^{-\omega_{x,3}x - \omega_{y,3}y - b_3}, \\ \phi_4 &= 2\omega_{2,f}\omega_{x,2}^2 + \omega_{3,f}\omega_{x,3}^2\phi_3, \\ \phi_5 &= (2\omega_{2,f}(\omega_{x,2}x + \omega_{y,2}y + b_2)\omega_{x,2} - \omega_{3,f}\omega_{x,3}\phi_3)^2. \end{aligned}$$

For the purpose of comprehensively analyzing the lump-stripe solution, systematic numerical studies were performed to explore both its dynamic properties and its evolutionary characteristics. Subsequently, the following parameter was selected and substituted into Eq (3.14):

$$\begin{aligned} &b_1 = 3, b_2 = 1, b_3 = 2, b_4 = 1, k_1 = 1, k_3 = 3, \\ &\omega_{1,f} = 1, \omega_{2,f} = 1, \omega_{3,f} = 2, \omega_{x,2} = 2, \omega_{x,3} = 3, \\ &\omega_{y,1} = 2, \omega_{y,2} = 3, \omega_{y,3} = 3. \end{aligned} \tag{3.15}$$

Figure 7 demonstrates the 3D plot with $t = 0$, the density plot with $t = 0$, and the line plot with $y = 0$ and $t = 0$. The substituted parameter is Eq (3.15). The 3D plot illustrates a complex structure with amplitude variations. The density plot presents the interaction between the lump and stripe features. The line graph shows the distinct peaks and decay patterns. The stripe-dominated background, together with the localized disturbance, illustrates how modulation and localization can coexist within an exact interaction solution.

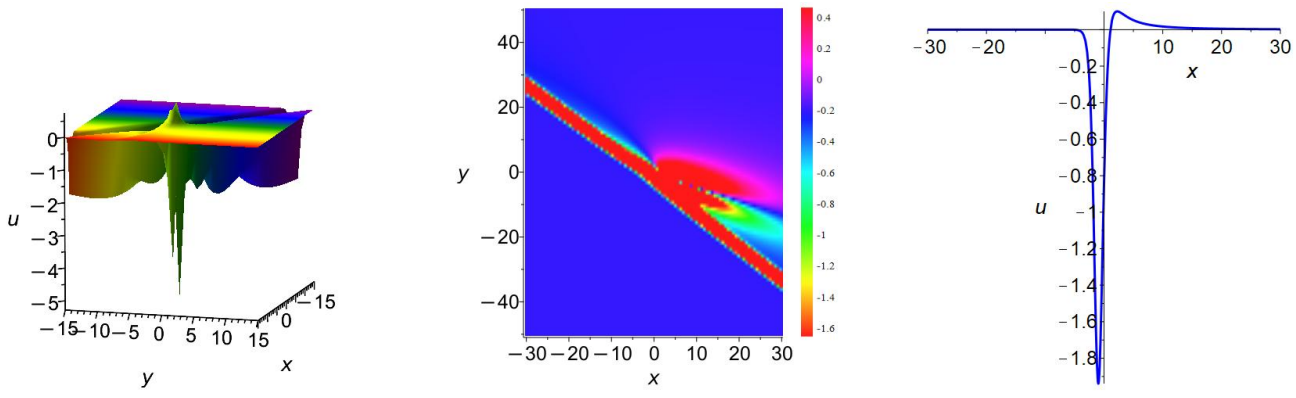

(a) 3D plot **(b)** density plot **(c)** line plot

Figure 7. The 3D plot, density plot, and line plot of lump-stripe solution.

By substituting *Case* 3 into Eq (3.8) and applying the bilinear transformation of Eq (2.5), the lump-

stripe solution of Eq (2.6) could be obtained as follows:

$$\begin{aligned} f &= \omega_{1,f}\phi_1^2 + \omega_{2,f}\phi_2^2 + \omega_{3,f}\phi_3 + b4, \\ u &= (k_2^2 - k_1^2)(\frac{\phi_4}{f} - \frac{\phi_5}{f^2}), \end{aligned} \tag{3.16}$$

where

$$\begin{aligned} \phi_1 &= \frac{3k_3k_4\omega_{y,1}^2 t}{2k_1\omega_{x,1}} + \omega_{x,1}x + \omega_{y,1}y + b_1, \\ \phi_2 &= \frac{3k_3k_4\omega_{y,1}^2\omega_{x,2}t}{2k_1\omega_{x,1}^2} + \omega_{x,1}x + \frac{\omega_{x,2}\omega_{y,1}y}{\omega_{x,1}} + b_2, \\ \phi_3 &= e^{-b_3}, \\ \phi_4 &= 2\omega_{1,f}\omega_{x,1}^2 + 2\omega_{2,f}\omega_{x,2}^2, \\ \phi_5 &= (2\omega_{1,f}\phi_1 + 2\omega_{2,f}\phi_2\omega_{x,2})^2. \end{aligned}$$

For the purpose of comprehensively analyzing the lump-stripe solution, systematic numerical studies were performed to explore both its dynamic properties and its evolutionary characteristics. Subsequently, the following parameter was selected and substituted into Eq (3.16):

$$\begin{aligned} &b_1 = 2, b_2 = 3, b_3 = 3, b_4 = 1, k_1 = 3, k_3 = 3, k_4 = 3, \\ &\omega_{1,f} = 3, \omega_{2,f} = 1, \omega_{3,f} = 3, \omega_{x,1} = 1, \omega_{x,2} = 3, \omega_{y,1} = 3. \end{aligned} \tag{3.17}$$

Figure 8 illustrates the 3D plot of this solution at different times, including $t = -1, t = 0$ and $t = 1$. The substituted parameter is shown in Eq (3.17). As time progressed from $t = -1$ to $t = 1$, the peaks exhibited changes in position. The three temporal snapshots emphasize the positional shift and the morphology variation of the interaction structure, which may be qualitatively relevant to observable propagation and pattern-evolution processes in dispersive media.

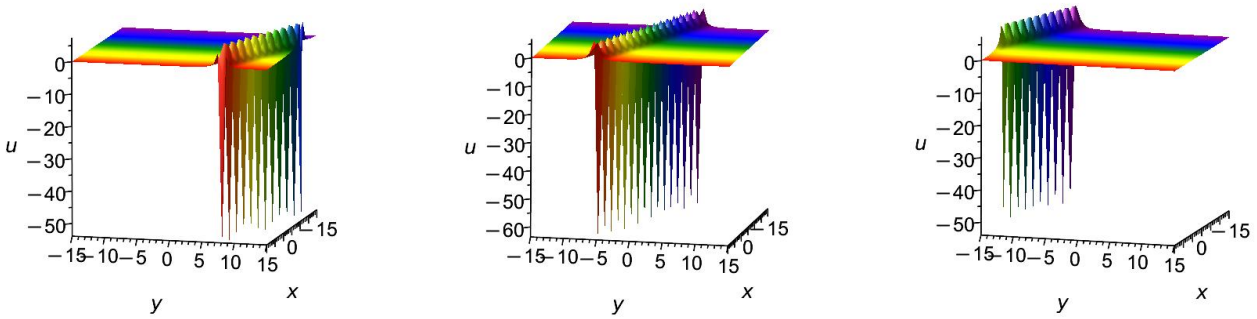

(a) t = -1 **(b)** t = 0 **(c)** t = 1

Figure 8. The 3D plots of lump-stripe-type solution.

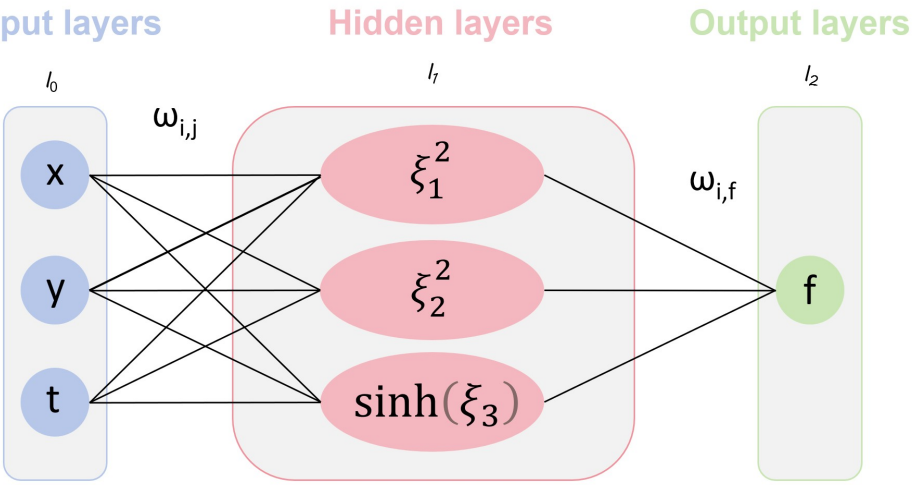

Figure 9. "3-3-1" Neural network model.

3.3. Lump-soliton solutions

The neural network structure was employed as follows:

$$\begin{aligned} f &= \omega_{1,f}F_1(\xi_1,\xi_2,\xi_3) + \omega_{2,f}F_2(\xi_1,\xi_2,\xi_3) + \omega_{3,f}F_3(\xi_1,\xi_2,\xi_3) + b_4,\\ \xi_1 &= \omega_{x,1}x + \omega_{y,1}y + \omega_{t,1}t + b_1,\\ \xi_2 &= \omega_{x,2}x + \omega_{y,2}y + \omega_{t,2}t + b_2,\\ \xi_3 &= \omega_{x,3}x + \omega_{y,3}y + \omega_{t,3}t + b_3, \end{aligned} \tag{3.18}$$

where b_k $(k = 1, 2, 3, 4)$ and $\omega_{i,j}$ $(i = x, y, t, 1, 2, 3$ and $j = 1, 2, 3, f)$ are real constants. The activation functions that remain to be identified are the functions $F_i(\xi_1, \xi_2, \xi_3)$ $(i = 1, 2, 3)$. The "3-3-1" neural network architecture is depicted in Figure 9.

$F_1(\xi_1, \xi_2, \xi_3) = \xi_1^2$, $F_2(\xi_1, \xi_2, \xi_3) = \xi_2^2$, and $F_3(\xi_1, \xi_2, \xi_3) = sinh(\xi_3)$ were chosen to act as activation functions. By substituting Eq (3.18) to Eq (2.6), a complex equation was obtained. By equating the coefficients to zero and ensuring $\omega_{1,f}, \omega_{2,f}, \omega_{3,f} \neq 0$, a system that consists of 24 coefficient equations was derived. With the use of Maple, two sets of solutions were obtained.

Case 1:

$$k_3 = 0, \omega_{1,f} = -\frac{\omega_{2,f}\omega_{x,2}^2}{\omega_{x,1}^2}, \omega_{t,1} = 0, \omega_{t,2} = 0, \omega_{t,3} = 0, \omega_{x,3} = 0. \tag{3.19}$$

Case 2:

$$k_2 = 0, \omega_{t,1} = \frac{3k_3k_4\omega_{y,1}^2}{2k_1\omega_{x,1}}, \omega_{t,2} = \frac{3k_3k_4\omega_{y,1}^2\omega_{x,2}}{2k_1\omega_{x,1}^2}, \omega_{t,3} = 0, \omega_{x,3} = 0, \omega_{y,2} = \frac{\omega_{x,2}\omega_{y,1}}{\omega_{x,1}}, \omega_{y,3} = 0. \tag{3.20}$$

By substituting *Case* 2 into Eq (3.18) and applying the bilinear transformation of Eq (2.5), the lump-soliton solution of Eq (2.6) could be obtained as follows:

$$\begin{aligned} f &= \omega_{1,f}\phi_1^2 + \omega_{2,f}\phi_2^2 + \omega_{3,f}\phi_3 + b_4,\\ u &= (k_2^2 - k_1^2)(\frac{\phi_3}{f} - \frac{\phi_4^2}{f^2}), \end{aligned} \tag{3.21}$$

where

$$\phi_1 = \frac{3tk_3k_4\omega_{y,1}^2}{2k_1\omega_{x,1}} + \omega_{x,1}x + \omega_{y,1}y + b_1,$$
$$\phi_2 = \frac{3tk_3k_4\omega_{y,1}^2\omega_{x,2}}{2k_1\omega_{x,1}^2} + \omega_{x,2}x + \frac{\omega_{x,2}\omega_{y,1}y}{\omega_{x,1}} + b_2,$$
$$\phi_3 = sinh(b_3),$$
$$\phi_4 = 2\omega_{1,f}\phi_1\omega_{x,1} + 2\omega_{2,f}\phi_2\omega_{x,2}.$$

For the purpose of comprehensively analyzing the lump-soliton solution, systematic numerical studies were performed to explore both its dynamic properties and its evolutionary characteristics. Subsequently, the following parameter was selected and substituted into Eq (3.21):

$$\begin{aligned} &b_1 = 1, b_2 = 2, b_3 = 2, b_4 = 2, k_1 = 1, k_3 = 1, k_4 = 2, \\ &\omega_{1,f} = 3, \omega_{2,f} = 1, \omega_{3,f} = 2, \omega_{x,1} = 3, \omega_{x,2} = 1, \omega_{y,1} = 3. \end{aligned} \tag{3.22}$$

Figure 10 shows the 3D plot with $t = 1$, the density plot with $t = 1$, and the line plot with $y = 0$, $t = -1$ (red), $t = 0$ (blue), and $t = 1$ (green). The substituted parameter is shown in Eq (3.22). The bimodal interference structure can be regarded as analogous to the evolutionary process following the collision of optical solitons and localized pulses in optical fibers. The bimodal interference pattern may be interpreted as a prototype interaction between a localized packet and a soliton-like carrier structure.

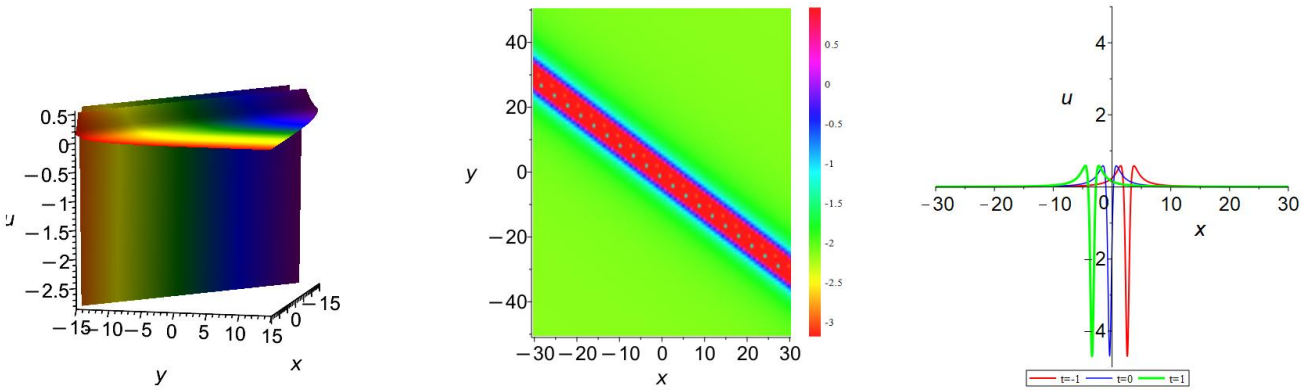

(a) 3D plot **(b)** density plot **(c)** line plot

Figure 10. The 3D plot, density plot, and line plot of lump-soliton-type solution.

4. Solutions under the architecture of a double hidden layers neural network

As discussed in this section, a neural network structure with a dual hidden layer was employed. Adding a hidden layer enriched the neural network and enhanced the network's ability to capture fine-grained and multi-scale patterns in the data. Through comprehensive computations, the exact analytical solutions of Eq (2.6) were generated as follows. Then, the solutions were visualized by means of three-dimensional plots, density plots, line plots, and evolution diagrams, through which further insights into the propagation and interaction properties of nonlinear waves were obtained.

4.1. General lump-stripe solutions

To generate the general lump-stripe solution, a dual hidden layer with a "3-2-3-1" architecture was implemented. This architecture included one input layer containing three neurons, two hidden layer consisting of two and three neurons, respectively, and one output layer. The "3-2-3-1" neural network structure was employed as follows:

$$f = \omega_{1,f}F_3(\xi_3,\xi_4,\xi_5) + \omega_{2,f}F_4(\xi_3,\xi_4,\xi_5) + \omega_{3,f}F_5(\xi_3,\xi_4,\xi_5) + b_6, \tag{4.1}$$

where

$$\begin{aligned}
\xi_1 &= \omega_{x,1}x + \omega_{y,1}y + \omega_{t,1}t + b_1,\\
\xi_2 &= \omega_{x,2}x + \omega_{y,2}y + \omega_{t,2}t + b_2,\\
\xi_3 &= \omega_{1,3}F_1(\xi_1,\xi_2) + \omega_{2,3}F_2(\xi_1,\xi_2) + b_3,\\
\xi_4 &= \omega_{1,4}F_1(\xi_1,\xi_2) + \omega_{2,4}F_2(\xi_1,\xi_2) + b_4,\\
\xi_5 &= \omega_{1,5}F_1(\xi_1,\xi_2) + \omega_{2,5}F_2(\xi_1,\xi_2) + b_5.
\end{aligned}$$

$F_1(\xi_1,\xi_2) = \xi_1$, $F_2(\xi_1,\xi_2) = \xi_2$, $F_3(\xi_3,\xi_4,\xi_5) = \xi_3^2$, $F_4(\xi_3,\xi_4,\xi_5) = \xi_4^2$, and $F_5(\xi_3,\xi_4,\xi_5) = cos(\xi_5)$ were chosen to act as activation functions. The "3-2-3-1" neural network architecture is depicted in Figure 11. By substituting Eq (4.1) into Eq (2.6), a complex equation was obtained. By equating the coefficients to zero and ensuring $\omega_{1,f}, \omega_{2,f}, \omega_{3,f} \neq 0$, a system that consists of 24 coefficient equations was derived. With the use of Maple, three sets of solutions were obtained.

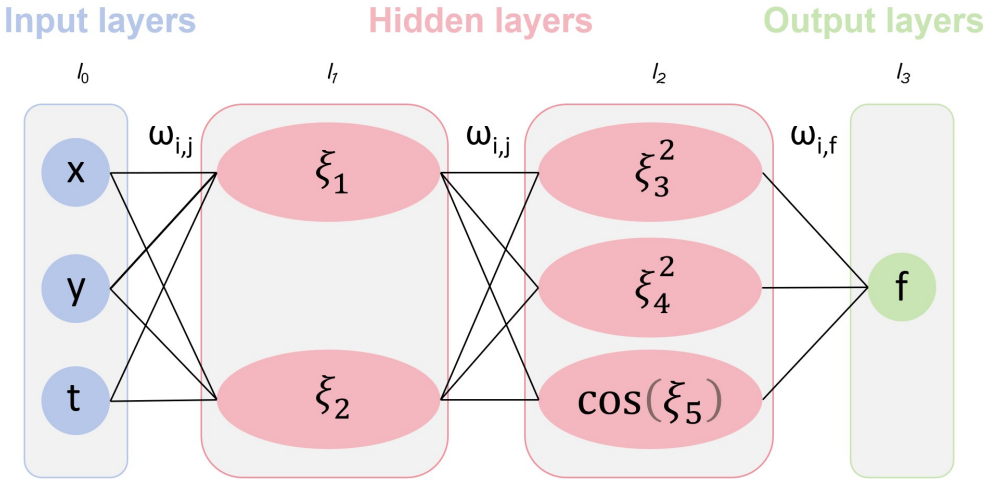

Figure 11. "3-2-3-1" Neural network model.

Case 1:

$$
\begin{aligned}
b_6 = &-\frac{1}{\omega_{1,3}}(b_1^2\omega_{1,3}^4\omega_{1,f} + b_1^2\omega_{1,3}^2\omega_{1,4}^2\omega_{2,f} + 2b_1b_2\omega_{1,3}^3\omega_{1,f}\omega_{2,3} + \\
&2b_1b_2\omega_{1,3}\omega_{1,4}^2\omega_{2,3}\omega_{2,f} + b_2^2\omega_{1,3}^2\omega_{1,f}\omega_{2,3}^2 + b_2^2\omega_{1,4}^2\omega_{2,3}^2\omega_{2,f} + \\
&2b_1b_3\omega_{1,3}^3\omega_{1,f} + 2b_1b_4\omega_{1,3}^2\omega_{1,4}\omega_{2,f} + 2b_2b_3\omega_{1,3}^2\omega_{1,f}\omega_{2,3} + \\
&2b_2b_4\omega_{1,3}\omega_{1,4}\omega_{2,3}\omega_{2,f} + b_3^2\omega_{1,3}^2\omega_{1,f} + b_4^2\omega_{1,3}^2\omega_{2,f}), \\
k_4 = 0, \omega_{2,4} = &\frac{\omega_{1,4}\omega_{2,3}}{\omega_{1,3}}, \\
\omega_{t,1} = &\frac{\omega_{2,3}k_2\omega_{x,2}^3}{\omega_{1,3}^3}(k_1^2\omega_{1,3}^2\omega_{2,5}^2 - 2k_1^2\omega_{1,3}\omega_{1,5}\omega_{2,3}\omega_{2,5} + k_1^2\omega_{1,5}^2\omega_{2,3}^2 - \\
&k_2^2\omega_{1,3}^2\omega_{2,5}^2 + 2k_2^2\omega_{1,3}\omega_{1,5}\omega_{2,3}\omega_{2,5} - k_2^2\omega_{1,5}^2\omega_{2,3}^2), \\
\omega_{t,2} = &\frac{k_2\omega_{x,2}^3}{\omega_{1,3}^3}(k_1^2\omega_{1,3}^2\omega_{2,5}^2 - 2k_1^2\omega_{1,3}\omega_{1,5}\omega_{2,3}\omega_{2,5} + k_1^2\omega_{1,5}^2\omega_{2,3}^2 - \\
&k_2^2\omega_{1,3}^2\omega_{2,5}^2 + 2k_2^2\omega_{1,3}\omega_{1,5}\omega_{2,3}\omega_{2,5} - k_2^2\omega_{1,5}^2\omega_{2,3}^2), \\
\omega_{x,1} = &-\frac{\omega_{2,3}\omega_{x,2}}{\omega_{1,3}}, \omega_{y,1} = -\frac{\omega_{2,3}\omega_{y,2}}{\omega_{1,3}}.
\end{aligned}
\tag{4.2}
$$

Case 2:

$$
k_2 = 0, k_4 = 0, \omega_{2,3} = -\frac{\omega_{1,3}^2\omega_{1,f}\omega_{x,1} + \omega_{1,4}^2\omega_{2,f}\omega_{x,1} + \omega_{1,4}\omega_{2,4}\omega_{2,f}\omega_{x,2}}{\omega_{1,3}\omega_{1,f}\omega_{x,2}}, \omega_{t,1} = 0, \omega_{t,2} = 0. \tag{4.3}
$$

Case 3:

$$
k_2 = 0, k_4 = 0, \omega_{1,3} = 0, \omega_{1,4} = 0, \omega_{t,1} = 0, \omega_{t,2} = 0. \tag{4.4}
$$

By substituting *Case* 1 into Eq (4.1) and applying the bilinear transformation of Eq (2.5), the special degenerate limit solution of Eq (2.6) could be obtained. Meanwhile, Equation (4.5) was selected and substituted into the resulting expression, thus yielding Eq. (4.6). The special degenerate limit solution is illustrated in Figure 12 as a 3D plot at $t = -1, t = 0$, and $t = 1$. As t transitioned from -1 to 1, distinct evolutions could be observed. As t shifted from -1 to 1, the 3D plots exhibited distinct and dynamic changes in the amplitude distribution. At $t = -1$, the amplitude was fairly localized, thereby concentrating its strong values in a particular area of the $x - y$ plane. The peak heights were notable, while their spatial coverage was limited, thus implying a highly focused dynamic condition. At $t = 0$, the amplitude spread much more widely across the $x - y$ plane, thus forming a far more complex structure with numerous peaks of different heights. This phase presented a rich, multimode pattern, thus suggesting that the underlying wave field underwent diversification and expansion in its spatial dynamics. At $t = 1$, the amplitude distribution became more scattered again, with the intensity of the peaks and their overall spatial range showing noticeable differences compared to both $t = -1$ and $t = 0$. Under certain admissible parameter choices, this degenerate limit can generate strongly amplified profiles. Since the variables in the present study are not experimentally calibrated, these large values are only interpreted as normalized exact-solution amplitudes, not as direct physical measurements. Therefore, the significance of this case lies in demonstrating the admissible analytical

richness of the reduced model, rather than in asserting a specific real-world amplitude prediction.

$$\begin{aligned} &b_1 = 3, b_2 = 3, b_3 = 2, b_4 = 1, b_5 = 2, k_1 = 1, k_2 = 2, k_3 = 3, \\ &\omega_{1,3} = 3, \omega_{1,4} = 3, \omega_{1,5} = 2, \omega_{1,f} = 1, \omega_{2,3} = 1, \omega_{2,5} = 3, \omega_{2,f} = 3, \\ &\omega_{3,f} = 2, \omega_{x,2} = 3, \omega_{y,2} = 1. \end{aligned} \tag{4.5}$$

$$\begin{aligned} f &= 2cos(2058t + 7x + \frac{7y}{3} + 17), \\ u &= -147 - \frac{147sin^2(2058t + 7x + \frac{7y}{3} + 17)}{cos^2(2058t + 7x + \frac{7y}{3} + 17)}. \end{aligned} \tag{4.6}$$

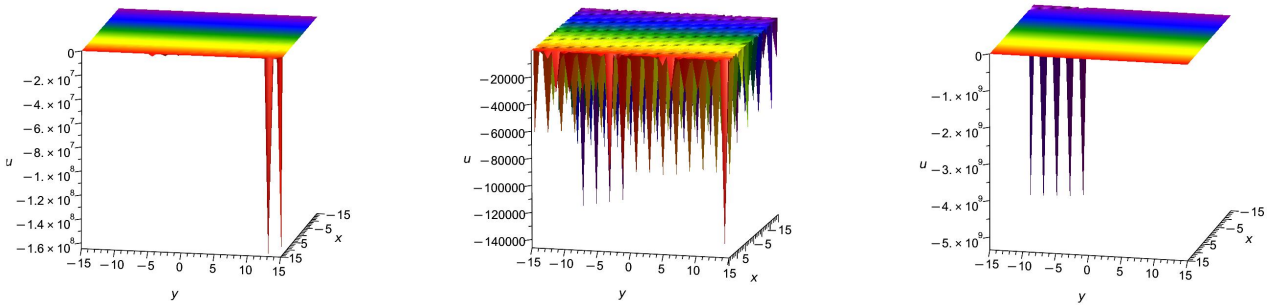

(a) t = -1 **(b)** t = 0 **(c)** t = 1

Figure 12. The 3D plots of a special degenerate limit solution.

By substituting *Case* 2 into Eq (4.1) and applying the bilinear transformation of Eq (2.5), the general lump-stripe solution of Eq (2.6) could be obtained as follows:

$$\begin{aligned} f &= \omega_{1,f}(\phi_1\omega_{1,3} - \frac{\phi_2\phi_3}{\phi_4} + b_3)^2 + \omega_{2,f}(\phi_1\omega_{1,4} + \phi_2\omega_{2,4} + b_4)^2 + \\ &\quad \omega_{3,f}cos(\phi_1\omega_{1,5} + \phi_2\omega_{2,5} + b_5) + b_6, \\ u &= (k_2^2 - k_1^2)((2\omega_{1,f}(\omega_{x,1}\omega_{1,3} - \frac{\phi_3}{\omega_{1,3}\omega_{1,f}})^2 + \\ &\quad 2\omega_{2,f}\phi_5^2 - \omega_{3,f}\phi_6^2 cos(\phi_1\omega_{1,5} + \phi_2\omega_{2,5} + b_5))/f \\ &\quad - (2\omega_{1,f}(\phi_1\omega_{1,3} - \frac{\phi_2\phi_3}{\phi_4} + b_3)(\omega_{x,1}\omega_{1,3} - \frac{\phi_3}{\omega_{1,3}\omega_{1,f}}) \\ &\quad + 2\omega_{2,f}(\phi_1\omega_{1,4} + \phi_2\omega_{2,4} + b_4)\phi_5 - \omega_{3,f}\phi_6 sin(\phi_1\omega_{1,5} + \phi_2\omega_{2,5} + b_5))^2/f^2), \end{aligned} \tag{4.7}$$

where

$$\begin{aligned}
\phi_1 &= \omega_{x,1}x + \omega_{y,1}y + b_1,\\
\phi_2 &= \omega_{x,2}x + \omega_{y,2}y + b_2,\\
\phi_3 &= \omega_{1,3}^2\omega_{1,f}\omega_{x,1} + \omega_{1,4}^2\omega_{2,f}\omega_{x,1} + \omega_{1,4}\omega_{2,4}\omega_{2,f}\omega_{x,2},\\
\phi_4 &= \omega_{1,3}\omega_{1,f}\omega_{x,2},\\
\phi_5 &= \omega_{x,1}\omega_{1,4} + \omega_{x,2}\omega_{2,4},\\
\phi_6 &= \omega_{x,1}\omega_{1,5} + \omega_{x,2}\omega_{2,5}.
\end{aligned}$$

For the purpose of comprehensively analyzing the general lump-stripe solution, systematic numerical studies were performed to explore both its dynamic properties and its evolutionary characteristics. Subsequently, the following parameter was selected and substituted into Eq (4.7):

$$\begin{aligned}
&b_1 = 2, b_2 = 2, b_3 = 1, b_4 = 2, b_5 = 3, b_6 = 3, k_1 = 1, k_3 = 2,\\
&\omega_{1,3} = 2, \omega_{1,4} = 1, \omega_{1,5} = 2, \omega_{1,f} = 2, \omega_{2,4} = 1, \omega_{2,5} = 1, \omega_{2,f} = 1,\\
&\omega_{3,f} = 1, \omega_{x,1} = 2, \omega_{x,2} = 3, \omega_{y,1} = 2, \omega_{y,2} = 2.
\end{aligned} \tag{4.8}$$

Figure 13 shows the 3D plot with $t = 0$, the density plot with $t = 0$, and the line plot with $y = 0$ and $t = 0$. The substituted parameter is shown in Eq (4.8). The density plot highlights a localized concentration zone embedded in a periodic stripe background, thus illustrating a representative localization-modulation interaction pattern.

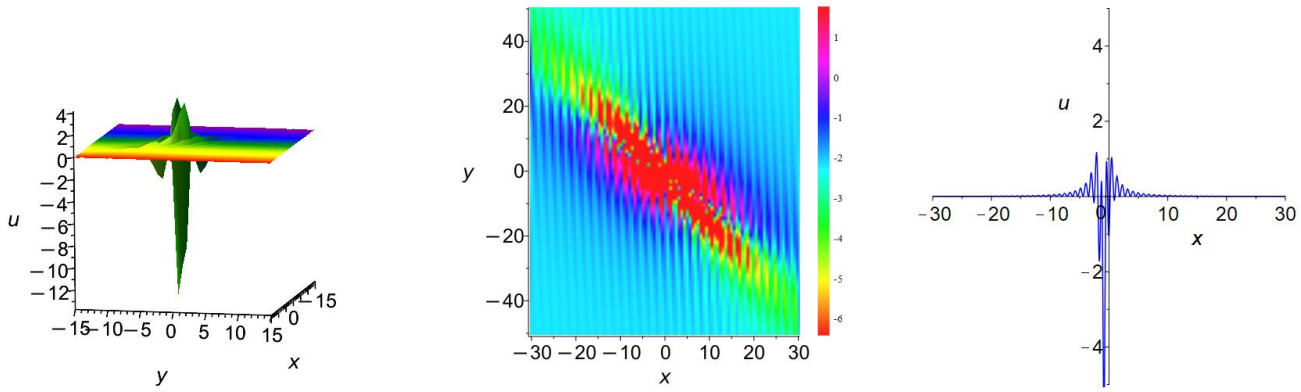

(a) 3D plot **(b)** density plot **(c)** line plot

Figure 13. The 3D plot, density plot, and line plot of general lump-stripe solution.

By substituting *Case* 3 into Eq (4.1) and applying the bilinear transformation of Eq (2.5), the general lump-stripe solution of Eq (2.6) could be obtained as follows:

$$\begin{aligned}
f &= \omega_{1,f}(\phi_1\omega_{2,3} + b_3)^2 + \omega_{2,f}(\phi_1\omega_{2,4} + b_4)^2 +\\
&\quad \omega_{3,f}cos(\phi_2\omega_{1,5} + \phi_1\omega_{2,5} + b_5) + b_6,\\
u &= (k_2^2 - k_1^2)(\frac{(\phi_3 + \phi_4 - \omega_{3,f}\phi_5^2 cos(\phi_2\omega_{1,5} + \phi_1\omega_{2,5} + b_5))}{f}\\
&\quad - (2\omega_{1,f}(\phi_1\omega_{2,3} + b_3)\omega_{x,2}\omega_{2,3} + 2\omega_{2,f}(\phi_1\omega_{2,4} + b_4)\omega_{x,2}\\
&\quad \omega_{2,4} - \omega_{3,f}\phi_5 sin(\phi_2\omega_{1,5} + \phi_1\omega_{2,5} + b_5))^2/f^2),
\end{aligned} \tag{4.9}$$

where

$$\begin{aligned}
\phi_1 &= x\omega_{x,2} + \omega_{y,2}y + b_2,\\
\phi_2 &= x\omega_{x,1} + \omega_{y,1}y + b_1,\\
\phi_3 &= 2\omega_{1,f}\omega_{x,2}^2\omega_{2,3}^2,\\
\phi_4 &= 2\omega_{2,f}\omega_{x,2}^2\omega_{2,4}^2,\\
\phi_5 &= \omega_{x,1}\omega_{1,5} + \omega_{x,2}\omega_{2,5}.
\end{aligned}$$

For the purpose of comprehensively analyzing the general lump-stripe solution, systematic numerical studies were performed to explore both its dynamic properties and its evolutionary characteristics. Subsequently, the following parameter was selected and substituted into Eq (4.9):

$$\begin{aligned}
&b_1 = 2, b_2 = 2, b_3 = 2, b_4 = 3, b_5 = 1, b_6 = 3, k_1 = 3,\\
&k_3 = 3, \omega_{1,5} = 1, \omega_{1,f} = 3, \omega_{2,3} = 1, \omega_{2,4} = 2, \omega_{2,5} = 1,\\
&\omega_{2,f} = 2, \omega_{3,f} = 3, \omega_{x,1} = 1, \omega_{x,2} = 3, \omega_{y,1} = 2, \omega_{y,2} = 1.
\end{aligned} \tag{4.10}$$

Figure 14 illustrates the 3D plot with $t = 1$, the density plot with $t = 1$, and the line plot with $y = 0$ and $t = 0$. The substituted parameter is shown in Eq (4.10). The superposition of localized and stripe-type components provide another exact prototype for the interaction between a concentrated packet and a periodic carrier mode.

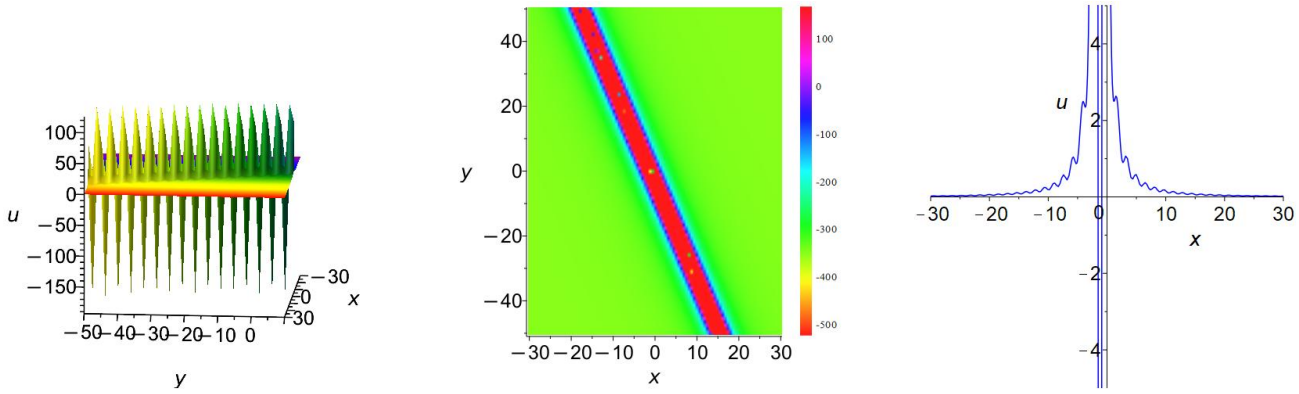

(a) 3D plot **(b)** density plot **(c)** line plot

Figure 14. The 3D plot, density plot, and line plot of general lump-stripe-type solution.

4.2. General lump-soliton solutions

The "3-2-3-1" neural network structure was employed as follows:

$$f = \omega_{1,f}F_3(\xi_3, \xi_4, \xi_5) + \omega_{2,f}F_4(\xi_3, \xi_4, \xi_5) + \omega_{3,f}F_5(\xi_3, \xi_4, \xi_5) + b_6, \tag{4.11}$$

where

$$\begin{aligned}
\xi_1 &= \omega_{x,1}x + \omega_{y,1}y + \omega_{t,1}t + b_1,\\
\xi_2 &= \omega_{x,2}x + \omega_{y,2}y + \omega_{t,2}t + b_2,\\
\xi_3 &= \omega_{1,3}F_1(\xi_1, \xi_2) + \omega_{2,3}F_2(\xi_1, \xi_2) + b_3,\\
\xi_4 &= \omega_{1,4}F_1(\xi_1, \xi_2) + \omega_{2,4}F_2(\xi_1, \xi_2) + b_4,\\
\xi_5 &= \omega_{1,5}F_1(\xi_1, \xi_2) + \omega_{2,5}F_2(\xi_1, \xi_2) + b_5.
\end{aligned}$$

$F_1(\xi_1,\xi_2)=\xi_1$, $F_2(\xi_1,\xi_2)=\xi_2$, $F_3(\xi_3,\xi_4,\xi_5)=\xi_3^2$, $F_4(\xi_3,\xi_4,\xi_5)=\xi_4^2$, and $F_5(\xi_3,\xi_4,\xi_5)=sinh(\xi_5)$ were chosen to act as the activation functions. The "3-2-3-1" neural network architecture is depicted in Figure 15. By substituting Eq (4.11) to Eq (2.6), a complex equation was obtained. By equating the coefficients to zero and ensuring $\omega_{1,f},\omega_{2,f},\omega_{3,f}\neq 0$, a system of 24 coefficient equations is derived. With the use of Maple, two sets of solutions were obtained.

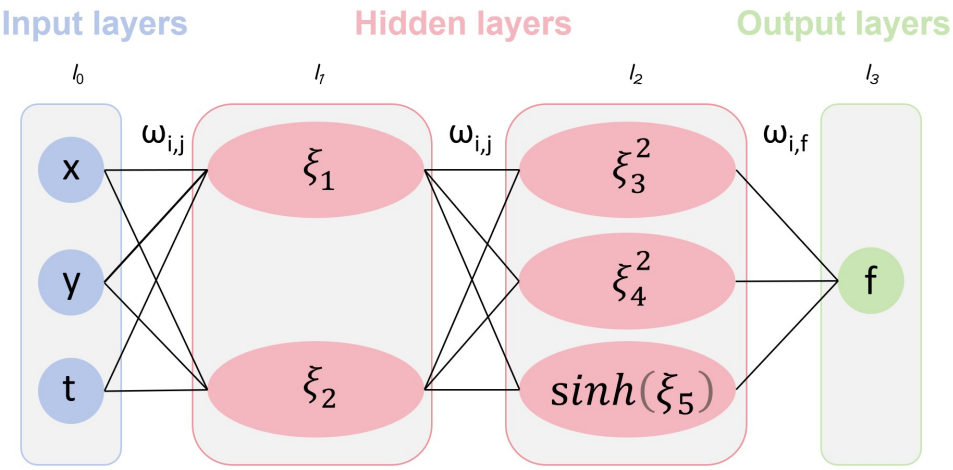

Figure 15. "3-2-3-1" Neural network model.

Case 1:

$$b_3=-b_1\omega_{1,3}-\omega_{2,3}b_2, b_4=-b_1\omega_{1,4}-b_2\omega_{2,4}, b_6=0, k_4=0, \omega_{1,f}=-\frac{\omega_{2,f}\omega_{1,4}^2}{\omega_{1,3}^2},$$
$$\omega_{t,1}=k_2\omega_{1,5}^2\omega_{x,1}^3(k_1^2-k_2^2), \omega_{t,2}=0, \omega_{x,1}=\omega_{x,1}, \omega_{x,2}=0, \omega_{y,2}=0. \tag{4.12}$$

Case 2:

$$k_2=0, k_4=0, \omega_{2,3}=-\frac{\omega_{1,3}^2\omega_{1,f}\omega_{x,1}+\omega_{1,4}^2\omega_{2,f}\omega_{x,1}+\omega_{1,4}\omega_{2,4}\omega_{2,f}\omega_{x,2}}{\omega_{1,3}\omega_{1,f}\omega_{x,2}}, \omega_{t,1}=0, \omega_{t,2}=0. \tag{4.13}$$

By substituting *Case* 1 into Eq (4.11) and applying the bilinear transformation of Eq (2.5), the general lump-soliton solution of Eq (2.6) could be obtained as follows:

$$\begin{aligned} f&=-\frac{\omega_{2,f}\omega_{1,4}^2\phi_1^2}{\omega_{1,3}^2}+\omega_{2,f}\phi_2^2+\omega_{3,f}sinh(\phi_3),\\ u&=(k_2^2-k_1^2)(\frac{\omega_{3,f}\omega_{x,1}^2\omega_{1,5}^2sinh(\phi_3)}{f}-(-\frac{2\omega_{2,f}\omega_{1,4}^2\phi_1\omega_{x,1}}{\omega_{1,3}}+\\ &\quad 2\omega_{2,f}\phi_2\omega_{x,1}\omega_{1,4}+\omega_{3,f}\omega_{x,1}\omega_{1,5}cosh(\phi_3))^2/f^2), \end{aligned} \tag{4.14}$$

where

$$\begin{aligned} \phi_1&=(tk_2\omega_{1,5}^2\omega_{x,1}^3(k_1^2-k_2^2)+\omega_{x,1}x+\omega_{y,1}y+b_1)\omega_{1,3}-b_1\omega_{1,3},\\ \phi_2&=(tk_2\omega_{1,5}^2\omega_{x,1}^3(k_1^2-k_2^2)+\omega_{x,1}x+\omega_{y,1}y+b_1)\omega_{1,4}-b_1\omega_{1,4},\\ \phi_3&=(tk_2\omega_{1,5}^2\omega_{x,1}^3(k_1^2-k_2^2)+\omega_{x,1}x+\omega_{y,1}y+b_1)\omega_{1,5}+b_2\omega_{2,5}+b_5. \end{aligned}$$

For the purpose of comprehensively analyzing the general lump-soliton solution, systematic numerical studies were performed to explore both its dynamic properties and its evolutionary characteristics. Subsequently, the following parameter was selected and substituted into Eq (4.14):

$$\begin{aligned} &b_1 = 2, b_2 = 3, b_5 = 1, k_1 = 1, k_2 = 3, k_3 = 1, \omega_{1,3} = 1, \\ &\omega_{1,4} = 2, \omega_{1,5} = 1, \omega_{2,3} = 1, \omega_{2,4} = 3, \omega_{2,5} = 2, \omega_{2,f} = 3, \\ &\omega_{3,f} = 3, \omega_{x,1} = 2, \omega_{y,1} = 3. \end{aligned} \tag{4.15}$$

Figure 16 demonstrates the 3D plot with $t = 0$, the density plot with $t = 0$, and the line plot with $y = 0$ and $t = 0$. The substituted parameter is shown in Eq (4.15). The 3D plot displays a structured spatial morphology with orderly distributed vertical features, while the density plot presents a distinct linear energy concentration zone. The line graph further reveals sharp waveform variations near the origin. The ordered vertical structures and narrow concentration band indicate a structured lump-soliton-type interaction pattern under the double-hidden-layer architecture.

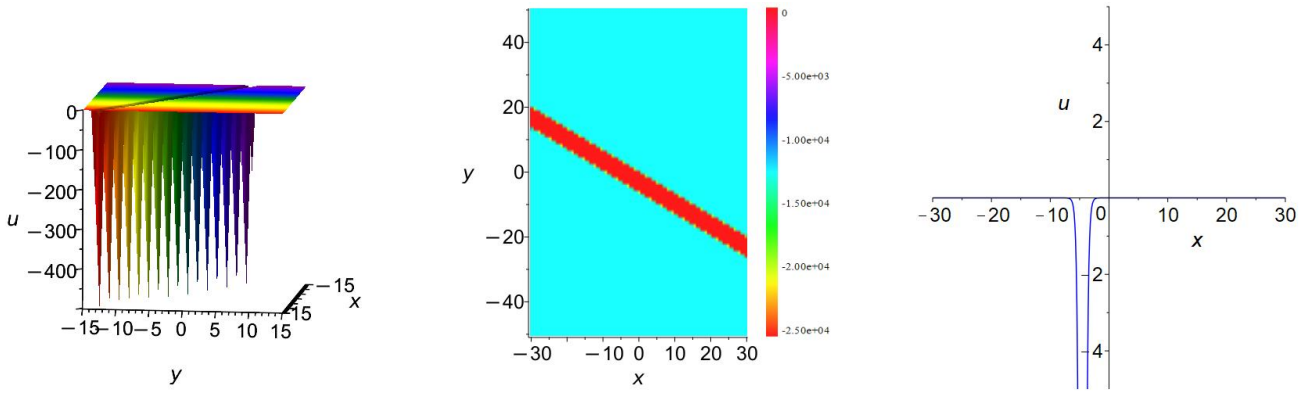

(a) 3D plot **(b)** density plot **(c)** line plot

Figure 16. The 3D plot, density plot, and line plot of general lump-soliton-type solution.

By substituting *Case* 2 into Eq (4.11) and applying the bilinear transformation of Eq (2.5), the general lump-soliton solution of Eq (2.6) could be obtained as follows:

$$\begin{aligned} f &= \omega_{1,f}(\phi_1\omega_{1,3} - \frac{\phi_2\phi_3}{\omega_{1,3}\omega_{1,f}\omega_{x,2}} + b_3)^2 + \omega_{2,f}(\phi_1\omega_{1,4} + \phi_2\omega_{2,4} + b_4)^2 \\ &\quad + \omega_{3,f}sinh(\phi_1\omega_{1,5} + \phi_2\omega_{2,5} + b_5) + b_6, \\ u &= (k_2^2 - k_1^2) \\ &\quad (\frac{2\omega_{1,f}(\omega_{x,1}\omega_{1,3} - \frac{\phi_3}{\omega_{1,3}\omega_{1,f}})^2 + 2\omega_{2,f}\phi_4^2 + \omega_{3,f}\phi_5^2 sinh(\phi_1\omega_{1,5} + \phi_2\omega_{2,5} + b_5)}{f} \\ &\quad - (2\omega_{1,f}(\phi_1\omega_{1,3} - \frac{\phi_2\phi_3}{\omega_{1,3}\omega_{1,f}\omega_{x,2}} + b_3)(\omega_{x,1}\omega_{1,3} - \frac{\phi_3}{\omega_{1,3}\omega_{1,f}}) \\ &\quad + 2\omega_{2,f}(\phi_1\omega_{1,4} + \phi_2\omega_{2,4} + b_4)\phi_4 \\ &\quad + \omega_{3,f}\phi_5 cosh(\phi_1\omega_{1,5} + \phi_2\omega_{2,5} + b_5))^2/f^2), \end{aligned} \tag{4.16}$$

where

$$\begin{aligned}
\phi_1 &= \omega_{x,1}x + \omega_{y,1}y + b_1,\\
\phi_2 &= x\omega_{x,2} + \omega_{y,2}y + b_2,\\
\phi_3 &= \omega_{1,3}^2\omega_{1,f}\omega_{x,1} + \omega_{1,4}^2\omega_{2,f}\omega_{x,1} + \omega_{1,4}\omega_{2,4}\omega_{2,f}\omega_{x,2},\\
\phi_4 &= \omega_{x,1}\omega_{1,4} + \omega_{x,2}\omega_{2,4},\\
\phi_5 &= \omega_{x,1}\omega_{1,5} + \omega_{x,2}\omega_{2,5}.
\end{aligned}$$

For the purpose of comprehensively analyzing the general lump-soliton solution, systematic numerical studies were performed to explore both its dynamic properties and its evolutionary characteristics. Subsequently, the following parameter was selected and substituted into Eq (4.16):

$$\begin{aligned}
&b_1 = 2, b_2 = 3, b_3 = 2, b_4 = 3, b_5 = 2, b_6 = 3, k_1 = 1, k_3 = 3, \omega_{1,3} = 2,\\
&\omega_{1,4} = 2, \omega_{1,5} = 1, \omega_{1,f} = 2, \omega_{2,4} = 2, \omega_{2,5} = 3, \omega_{2,f} = 3, \omega_{3,f} = 1, \omega_{x,1} = 3,\\
&\omega_{x,2} = 2, \omega_{y,1} = 3, \omega_{y,2} = 1.
\end{aligned} \tag{4.17}$$

Figure 17 demonstrates the 3D plot with $t = 0$, the density plot with $t = 0$, and the line plot with $y = 0$ and $t = 0$. The substituted parameter is Eq (4.17). The 3D plot exhibits a prominent central peak accompanied by secondary surrounding fluctuations. The density plot displays multiple diagonal energy distributions, and the line plot presents a sharp central peak with symmetric side structures. The central peak and diagonal side structures illustrate a more complex interaction morphology with simultaneous localization and sideband-type modulation.

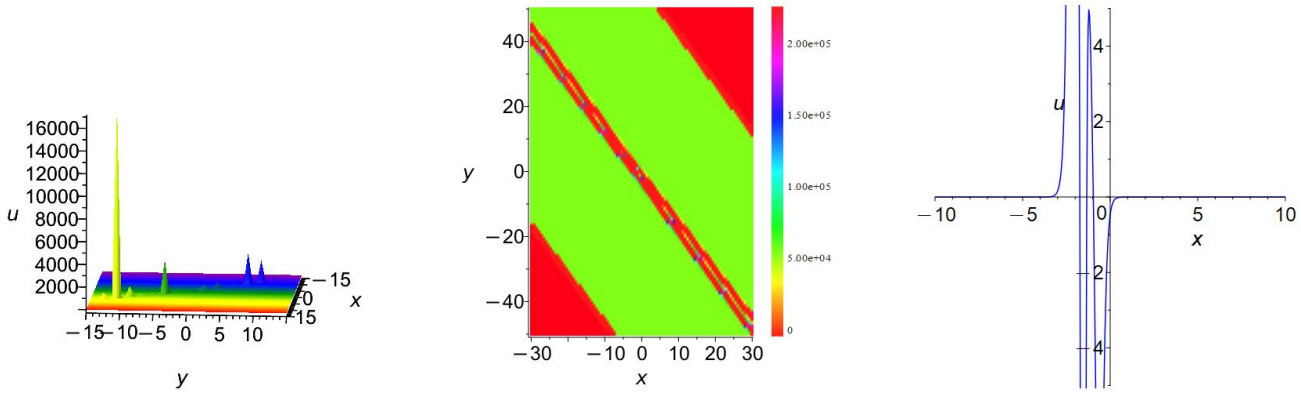

(a) 3D plot **(b)** density plot **(c)** line plot

Figure 17. The 3D plot, density plot, and line plot of general lump-soliton-type solution.

5. Auxiliary Duffing-based modulation diagnostic

One representative profile in Figure 12 exhibits a strongly amplified response under a particular admissible parameter set, which motivates a supplementary qualitative examination of irregular modulation. It should be emphasized that the Duffing oscillator used below is not derived from Eq (2.6), and the present subsection is not a standard chaos proof for the reduced Fokas equation. Unlike diagnostics directly constructed from trajectories of the governing system itself, the Duffing model is only introduced here as an external nonlinear benchmark for post-processing one selected

solution profile. Accordingly, the following discussion should be understood as an auxiliary qualitative comparison of modulation irregularity, rather than as a rigorous claim that the reduced Fokas equation itself is chaotic. In a damped elastic system, the potential energy function satisfies the following governing equation:

$$\frac{d^2X}{dt^2} + \alpha\frac{dX}{dt} + \beta X^3 = 0. \tag{5.1}$$

The Duffing oscillator is only used here as a classical auxiliary nonlinear benchmark. For certain forcing, damping, and initial-condition regimes, it may exhibit irregular or chaotic responses. In the present paper, its forced form is solely introduced for a qualitative comparison of the modulation sensitivity and irregularity, and not as evidence that Eq (2.6) itself possesses a rigorously established chaotic attractor. The governing equation will transform into the following:

$$\frac{d^2X}{dt^2} + \alpha\frac{dX}{dt} + \beta X^3 = \rho cost. \tag{5.2}$$

The parameters can be set to the following values:

$$\alpha = 0.05, \beta = 1, \rho = 7.5, \tag{5.3}$$

with the initial conditions

$$X'(0) = 1, X(0) = 1. \tag{5.4}$$

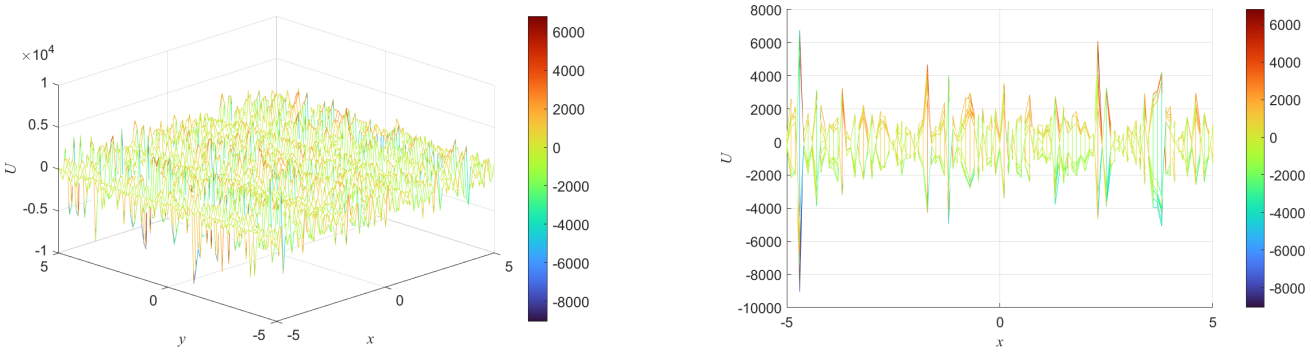

(a) Chaotic solution surface plot

(b) X-direction front view

Figure 18. Auxiliary Duffing-based modulation diagnostic: surface plot (a) and x-direction section (b).

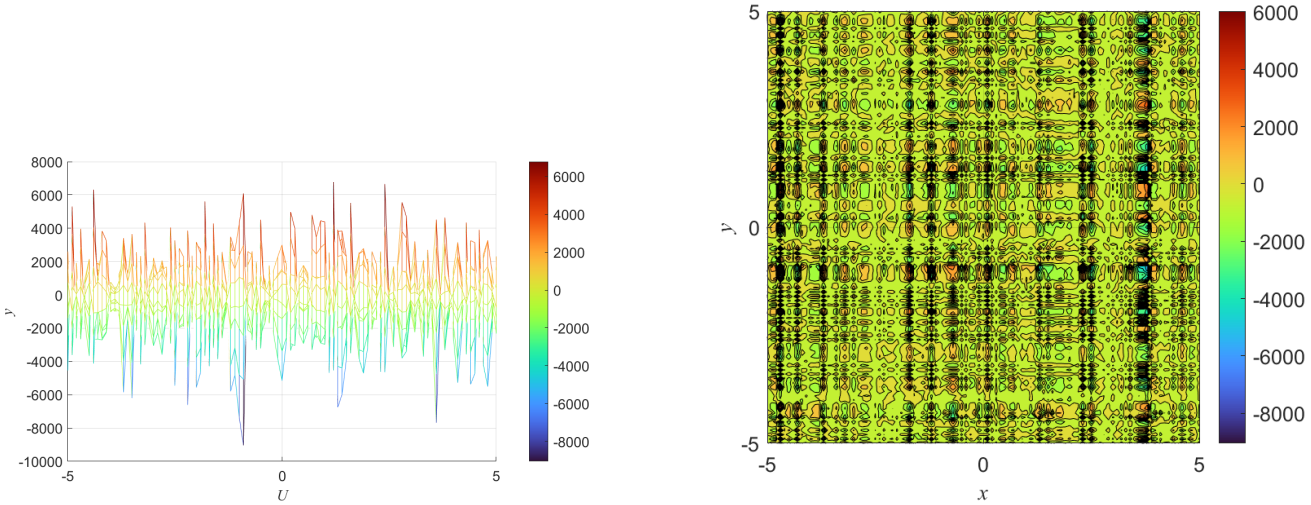

(a) Y-direction front view

(b) Contour plot

Figure 19. Auxiliary Duffing-based modulation diagnostic: y-direction section (a) and contour plot (b).

Figure 18(a) presents irregular and dense oscillating structures in a three-dimensional space. The amplitude of the solution randomly fluctuated within a large range, without obvious periodicity.

As shown in Figures 18(b) and 19(a), the curve of U with respect to x and y exhibited highly irregular oscillations. The amplitude ranged from $-10,000$ to 8000, and both the peak positions and oscillation frequencies were random.

As shown in Figure 19(b), the contour lines are extremely complex and highly intertwined. Different amplitude regions randomly overlap and its state randomly traverses most regions of the phase space, rather than being confined to a fixed sub-region.

These observations are only used here to visualize irregular modulation associated with one selected high-amplitude exact profile under an external nonlinear-oscillator comparison. They are not interpreted as a rigorous phase-space proof, Poincaré-type diagnostic, or Lyapunov-based demonstration of chaos for Eq (2.6).

6. Conclusions

In this work, the (4+1)-dimensional Fokas equation was studied through a reduction-plus-BNNM framework. By reducing the original equation to a (2+1)-dimensional bilinear form and combining it with symbolic coefficient matching under several architecture-guided trial-function constructions, multiple exact solution families were obtained under the "3-2-1", "3-3-1", and "3-2-3-1" configurations. These results include lump solutions, lump–stripe-type solutions, lump–soliton-type solutions, and representative high-amplitude patterns. The comparative analysis suggests that changes in the hidden-layer depth and the activation composition affect the admissible ansatz structure and the morphology of the resulting interaction profiles within this reduced Fokas-equation setting. In this sense, the present study not only provides additional exact solutions, but also provides an equation-specific comparison of how different BNNM architectures organize localized interaction patterns.

An auxiliary Duffing-based diagnostic was only included as a qualitative post-processing comparison for one selected high-amplitude profile, without claiming a rigorous chaos result for the reduced Fokas equation.

Overall, the results indicate that the BNNM framework offers a structured symbolic route to construct and compare the exact wave solutions of the reduced (4+1)-dimensional Fokas equation. Future work will focus on a stricter classification of degenerate and interaction-type profiles, a more systematic exploration of admissible parameter regimes, and extensions of the present framework to other higher-dimensional nonlinear evolution equations relevant to fluid dynamics, nonlinear optics, and related dispersive systems.

Author contributions

Conceptualization: Junjie Li. Investigation: Junjie Li, Pei Lin. Methodology: Junjie Li. Supervision: Junjie Li, Xin Zhen, Junjiang Zhong. Validation: Junjie Li, Pei Lin. Writing—original draft: Junjie Li, Pei Lin. Writing—review & editing: Junjie Li, Pei Lin, Xin Zhen, Junjiang Zhong.

Use of AI tools declaration

The authors declare they have not used Artificial Intelligence (AI) tools in the creation of this article.

Acknowledgments

This research was funded by the Natural Science Foundation of Xiamen, China (3502Z20227220), the Ministry of Education of China project on Humanities and Social Sciences (21YJC910011) and the Natural Science Foundation of Fujian Province of China (2023J011434, 2023J011433).

Conflict of interest

The authors declare there is no conflict of interest.

References

1. X. Y. Li, X. L. Yong, Y. H. Huang, Lump solutions to the (3+1)-dimensional Mel'nikov equation, *Adv. Appl. Math.*, **8** (2019), 1058–1063. https://doi.org/10.12677/aam.2019.86121
2. H. Yang, B. He, Bilinear bäcklund transformations, lump solutions and interaction solutions for the (4+1)-dimensional variable-coefficient Fokas equation, *Z. Angew. Math. Phys.*, **74** (2023), 155. https://doi.org/10.1007/s00033-023-02052-3
3. Y. Zhu, K. Li, C. Huang, Y. Xu, J. Zhong, J. Li, Abundant exact solutions of the fractional (3+1)-dimensional Yu–Toda–Sasa–Fukuyama (YTSF) equation using the Bell Polynomial-based neural network method, *Chaos, Solitons Fractals*, **196** (2025), 116333. https://doi.org/10.1016/j.chaos.2025.116333

4. Y. L. Liu, Z. Ma, R. Lei, Lump solution, interaction solution, and interference wave for the (3+1)-dimensional BKP-Boussinesq equation as well as analysis of BNNM model degradation, *Nonlinear Dyn.*, **112** (2024), 2837–2849. https://doi.org/10.1007/s11071-023-09169-0
5. M. Raissi, P. Perdikaris, G. E. Karniadakis, Physics-informed neural networks: A deep learning framework for solving forward and inverse problems involving nonlinear partial differential equations, *J. Comput. Phys.*, **378** (2019), 686–707. https://doi.org/10.1016/j.jcp.2018.10.045
6. R. K. Gupta, M. Kumar, Dynamical behavior of lump, breather and soliton solutions of time-fractional (3+1) d-ytsf equation with variable coefficients, *Nonlinear Dyn.*, **112** (2024), 8527–8538. https://doi.org/10.1007/s11071-024-09531-w
7. P. R. Kundu, M. R. A. Fahim, M. E. Islam, M. A. Akbar, The sine-Gordon expansion method for higher-dimensional NLEEs and parametric analysis, *Heliyon*, **7** (2021), e06459. https://doi.org/10.1016/j.heliyon.2021.e06459
8. H. Zhang, D. Y. Liu., Localized waves and interactions for the high dimensional nonlinear evolution equations, *Appl. Math. Lett.*, **102** (2020), 106102. https://doi.org/10.1016/j.aml.2019.106102
9. Y. Zhang, K. Dong, R. Jin, The Darboux transformation for the coupled Hirota equation, *Nonlinear Mod. Math. Phys.*, **1562** (2013), 249–256. https://doi.org/10.1063/1.4828697
10. W. X. Ma, Soliton solutions by means of Hirota bilinear forms, *Partial Differ. Equ. Appl. Math.*, **5** (2022), 100220. http://dx.doi.org/10.1016/j.padiff.2021.100220
11. Y. Yildirim, M. A. S. Murad, A. H. Arnous, A. Biswas, L. Moraru, Y. Yildirim, Quiescent optical soliton perturbation for fokas-lenells equation with nonlinear chromatic dispersion and generalized quadratic-cubic form of self-phase modulation structure, *Contemp. Math.*, **6** (2025), 2308–2338. https://doi.org/10.37256/cm.6220256359
12. D. V. Tanwar, M. Kumar, On lie symmetries and invariant solutions of broer–kaup–kupershmidt equation in shallow water of uniform depth, *J. Ocean. Eng. Sci.*, **9** (2024), 199–206. https://doi.org/10.1016/j.joes.2022.04.027
13. R. F. Zhang, M. C. Li, T. Fang, F. C. Zheng, S. Bilige, Multiple exact solutions for the dimensionally reduced p-gBKP equation via bilinear neural network method, *Mod. Phys. Lett. B*, **36** (2022), 2150590. https://doi.org/10.1142/s0217984921505904
14. L. Yang, B. Gao, The nondegenerate solitons solutions for the generalized coupled higher-order nonlinear Schrödinger equations with variable coefficients via the Hirota bilinear method, *Chaos, Solitons Fractals*, **184** (2024), 115009. https://doi.org/10.1016/j.chaos.2024.115009
15. M. Qasim, F. Yao, H. F. Ismael, M. Z. Baber, T. A. Sulaiman, Dynamics of N-soliton waves, lump-breathers, and M-lump collision with improved bilinear neural network method, *Eur. Phys. J. Plus*, **140** (2025), 815. https://doi.org/10.1140/epjp/s13360-025-06705-2
16. W. X. Ma, Trilinear equations, Bell polynomials, and resonant solutions, *Front. Math. China*, **8** (2013), 1139–1156. https://doi.org/10.1007/s11464-013-0319-5
17. Y. J. Shen, Y. T. Gao, X. Yu, G. Q. Meng, Y. Qin, Bell-polynomial approach applied to the seventh-order Sawada–Kotera–Ito equation, *Appl. Math. Comput.*, **227** (2014), 502–508. https://doi.org/10.1016/j.amc.2013.11.005

18. M. S. Ghayad, N. M. Badra, H. M. Ahmed, W. B. Rabie, Derivation of optical solitons and other solutions for nonlinear schrödinger equation using modified extended direct algebraic method, *Alexandria Eng. J.*, **64** (2023), 801–811. https://doi.org/10.1016/j.aej.2022.10.054

19. K. J. Wang, K. H. Yan, S. Li, Multi-rogue wave, generalized breathers wave, bell shape and singular wave solutions to the (3+1)-dimensional Yu-Toda-Sasa-Fukuyama equation, *Math. Methods Appl. Sci.*, **44** (2021), 14291–14306. https://doi.org/10.1002/mma.70663

20. K. J. Wang, K. H. Yan, J. Cheng, Y. B. Zheng, F. Shi, H. W. Zhu, et al., Bilinear form, Bäcklund transformation to the Kairat-II-X-extended equation: *N*-soliton, anti-kink soliton, novel soliton molecule, multi-lump and travelling wave solutions, *Mod. Phys. Lett. B*, **40** (2026), 2650057. https://doi.org/10.1142/S0217984926500570

21. K. J. Wang, Exploring the fractal exothermic reactions model with constant heat source and porous media via a novel fractal physics-informed neural networks method, *Fractals*, (2026), in press. https://doi.org/10.1142/S0218348X26500878

22. L. Lu, X. Meng, Z. Mao, G. E. Karniadakis, Deepxde: A deep learning library for solving differential equations, *SIAM Rev.*, **63** (2021), 208–228. https://doi.org/10.1137/19m1274067

23. Z. Li, N. Kovachki, K. Azizzadenesheli, B. Liu, K. Bhattacharya, A. Stuart, et al., Fourier neural operator for parametric partial differential equations, preprint, arXiv:2010.08895. https://doi.org/10.48550/arXiv.2010.08895

24. M. Raissi, P. Perdikaris, G. E. Karniadakis, Physics informed deep learning (part i): Data-driven solutions of nonlinear partial differential equations, preprint, arXiv:1711.10561. https://doi.org/10.48550/arXiv.1711.10561

25. R. F. Zhang, S. Bilige, Bilinear neural network method to obtain the exact analytical solutions of nonlinear partial differential equations and its application to p-gBKP equation, *Nonlinear Dyn.*, **95** (2019), 3041–3048. https://doi.org/10.1007/s11071-018-04739-z

26. R. F. Zhang, M. C. Li, J. Y. Gan, Q. Li, Z. Z. Lan, Novel trial functions and rogue waves of generalized breaking soliton equation via bilinear neural network method, *Chaos, Solitons Fractals*, **154** (2022), 111692. https://doi.org/10.1016/j.chaos.2021.111692

27. C. Huang, Y. Zhu, K. Li, J. Li, R. Zhang, M-lump solutions, lump-breather solutions, and N-soliton wave solutions for the KP-BBM equation via the improved bilinear neural network method using innovative composite functions, *Nonlinear Dyn.*, **112** (2024), 21355–21368. https://doi.org/10.1007/s11071-024-10122-y

28. K. J. Wang, Exploring exact wave solutions of the Cahn–Allen equation via a novel Bernoulli sub-equation neural networks method, *Mod. Phys. Lett. B*, **40** (2026), 2650062. https://doi.org/10.1142/S0217984926500624

29. J. M. Qiao, R. F. Zhang, R. X. Yue, H. Rezazadeh, A. R. Seadawy, Three types of periodic solutions of new (3+1)-dimensional Boiti–Leon–Manna–Pempinelli equation via bilinear neural network method, *Math. Methods Appl. Sci.*, **45** (2022), 5612–5621. https://doi.org/10.1002/mma.8131

30. Y. Zhang, Y. Zhang, C. M. Khalique, N. Bessaad, Novel hybrid solitary waves and shrunken-periodic solutions, solitary moiré pattern and conserved vectors of the (4 + 1)-Fokas equation, *Int. J. Geom. Methods Mod. Phys.*, **19** (2022), 2250195. https://doi.org/10.1142/S021988782250195X

31. M. Dargis, R. Ye, Miura transformation in bidifferential calculus and a vectorial Darboux transformation for the Fokas-Lenells equation, *J. Phys. A: Math. Theor.*, **58** (2025), 295201. https://doi.org/10.1088/1751-8121/adebc6
32. R. Ye, Y. Zhang, A vectorial Darboux transformation for the Fokas–Lenells system, *Chaos, Solitons Fractals*, **169** (2023), 113233. https://doi.org/10.1016/j.chaos.2023.113233
33. Y. L. Cao, J. He, Y. Cheng, D. Mihalache, Reduction in the (4+1)-dimensional Fokas equation and their solutions, *Nonlinear Dyn.*, **99** (2020), 3013–3028. https://doi.org/10.1007/s11071-020-05485-x
34. Y. L. Cao, J. S. He, Y. Cheng, The attenuation ripple waves within the (3 + 1)-dimensional Kadomtsev–Petviashvili equation, *Nonlinear Dyn.*, **114** (2026), 341. https://doi.org/10.1007/s11071-026-12218-z
35. Y. L. Cao, J. S. He, Y. Cheng, New localized wave structures in the Maccari system, *Nonlinear Dyn.*, **112** (2024), 22201–22219. https://doi.org/10.1007/s11071-024-10165-1
36. Y. L. Cao, J. S. He, Y. Cheng, Doubly localized two-dimensional rogue waves generated by resonant collision in Maccari system, *Stud. Appl. Math.*, **152** (2024), 648–672. https://doi.org/10.1111/sapm.12657
37. Y. L. Cao, J. S. He, Y. Cheng, The partial-rogue ripple solutions of nonlocal Kadomtsev-Petviashvili equation, *Physica D*, **458** (2024), 133990. https://doi.org/10.1016/j.physd.2023.133990
38. S. Kumar, B. Mohan, A direct symbolic computation of center-controlled rogue waves to a new Painlevé-integrable (3+1)-D generalized nonlinear evolution equation in plasmas, *Nonlinear Dyn.*, **111** (2023), 16395–16405. https://doi.org/10.1007/s11071-023-08683-5
39. C. X. Zhao, Lump-type wave solutions to the (4+1)-dimensional Fokas equation, *Eng. Lett.*, **33** (2025), 3640–3647.
40. A. S. Fokas, Integrable nonlinear evolution partial differential equations in 4+2 and 3+1 dimensions, *Phys. Rev. Lett.*, **96** (2006), 190201. https://doi.org/10.1103/PhysRevLett.96.190201

AIMS Press